Thin Solid Films 598 (2016) 315–334

Contents lists available at ScienceDirect

Thin Solid Films

journal homepage: www.elsevier.com/locate/tsf

Critical review

Atmospheric pressure plasmas for surface modification of flexible and printed electronic devices: A review

Kyong Nam Kim [a], Seung Min Lee [a], Anurag Mishra [a], Geun Young Yeom [a,b,*]

[a] Department of Materials Science and Engineering, Sungkyunkwan University, Suwon, Gyeonggi-do 440-746, South Korea
[b] SKKU Advanced Institute of Nano Technology (SAINT), Sungkyunkwan University, Suwon, Gyeonggi-do 440-746, South Korea

ARTICLE INFO

Available online 27 May 2015

Keywords:
Atmospheric pressure plasma
Flexible electronic devices
Surface activation and treatment surface texturing
Sintering

ABSTRACT

Recently, non-equilibrium atmospheric pressure plasma, especially those operated at low gas temperatures, have become a topic of great interest for the processing of flexible and printed electronic devices due to several benefits such as the reduction of process and reactor costs, the employment of easy-to-handle apparatuses and the easier integration into continuous production lines. In this review, several types of typical atmospheric pressure plasma sources have been addressed, and the processes including surface treatment, texturing and sintering for application to flexible and printed electronic devices have been discussed.

© 2015 Elsevier B.V. All rights reserved.

Contents

1. Introduction . . . 315
2. Atmospheric pressure plasma sources . . . 315
 2.1. Dielectric barrier discharges (DBDs) . . . 316
 2.2. Atmospheric pressure plasma jets and plasma torches . . . 317
 2.3. Corona discharges . . . 317
3. APP applications for flexible and printed electronics devices . . . 318
 3.1. Surface treatment and activation . . . 318
 3.2. Surface etching and texturing . . . 322
 3.3. Low temperature plasma sintering . . . 325
 3.4. Deposition on plastic substrates . . . 330
4. Conclusion . . . 333
Acknowledgments . . . 334
References . . . 334

1. Introduction

In recent years, there has been an increasing interest in flexible and printed electronic devices due to significant advantages including high process efficiency, large scale patternability, environmental friendliness, etc. [1–4]. The conventional low pressure plasma system as a depositional, etching, or surface modification tool for flexible and printed electronics poses economic and integration problems due the complexity arising from the necessity of vacuum systems, which makes it hard to integrate into a continuous production line. In this context, atmospheric pressure plasma (APP) technologies attract growing interest in the field of surface processing of flexible materials due to the absence of vacuum equipment, which results in several benefits such as the reduction of process and reactor costs, the employment of easy-to-handle apparatuses, and the easier integration into continuous production lines. [3–5]

This article summarizes the various types of APP sources. We also discuss the surface treatment, activation, texturing, and sintering of flexible substrates achieved using APP technology.

2. Atmospheric pressure plasma sources

APP sources can be classified on the basis of key parameters such as driving frequency, ignition type, and gas temperature, etc.

* Corresponding author at: Department of Materials Science and Engineering, Sungkyunkwan University, Suwon, Gyeonggi-do 440-746, South Korea.
E-mail address: gyyeom@skku.edu (G.Y. Yeom).

http://dx.doi.org/10.1016/j.tsf.2015.05.035
0040-6090/© 2015 Elsevier B.V. All rights reserved.

On the basis of driving frequency or the method for voltage application to generate the plasma, APP sources can be divided as follows: (1) direct current (DC) discharges, (2) alternating current (AC) discharges, (3) radio frequency (RF) discharges and (4) microwave (MW) discharges [4–6].

APP sources operating at DC or low-frequency (AC) are characterized by a low electron temperature, low gas temperature, and a high breakdown voltage of a few kV. The discharges can also be used in a pulsed mode which provides more flexibility to tailor the discharge properties and enables the injection of higher power with a corresponding higher degree of ionization. APP discharges operating at radio frequency are characterized by higher plasma density and lower breakdown voltage. However, APPs operating at the microwave frequency of 2.45 GHz exhibit a high electron temperature and a high gas temperature [6].

Another way to classify APP sources is by electrode configuration. One such APP source is the dielectric barrier discharge (DBD) [3,5,6]. DBD sources have a simple electrode configuration and are easily implemented to produce plasmas. In addition to DBD APPs, other types of APP sources such as corona discharges and plasma jets are widely investigated. For the operation of the APP sources, high flow rates (slm scale) of He, Ar, or N_2 are generally used as the ignition and stabilization gas and small amounts of other reactive gasses (sccm scale) such as O_2, CF_4, CH_4, etc. are added for the required surface reaction during the APP operation.

2.1. Dielectric barrier discharges (DBDs)

Dielectric discharges are generated between two electrodes, in which at least one of the electrodes is covered by a dielectric material, thickness ranging from a μm to a few mm, to limit the discharge current. These discharges are typically operated in a non-thermal uniform glow-type plasma regime. The separation between two DBD electrodes varies from micrometers to centimeters and depends upon the gas mixture used and the applied voltage. One of the advantages of DBD discharges is manifold symmetry and, therefore, these discharges can be used for large-area surface modification. DBD discharges are typically operated at a frequency range from few hertz (AC) to megahertz (RF) and at an electrode voltage of few thousand volts [3,7,8].

There are various designs, constructions, electrode shapes, and dielectric barrier materials used in DBD sources. Depending upon the application, the DBD electrode shapes may be a planar or coplanar array. Typical DBD source designs are in Fig. 1. Fig. 1(a) is a simple planar direct parallel plate DBD system investigated for various substrate

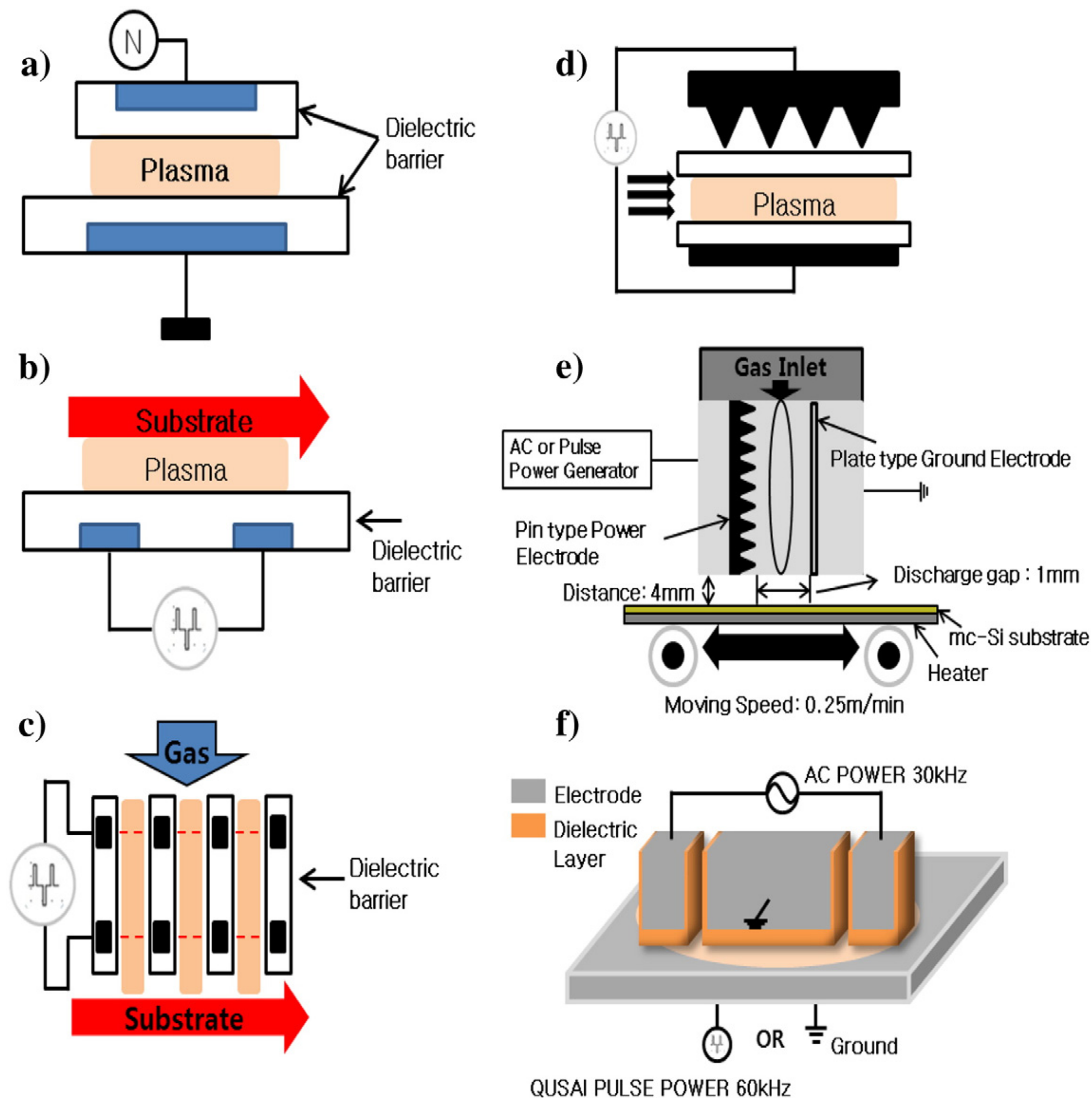

Fig. 1. (a) A simple planar direct DBD source, (b) surface-barrier DBD source, and (c) remote DBD source. Modifications of these sources are (d) multi-pin direct DBD source, (e) multi-pin remote DBD source, and a double-discharge DBD source composed of direct DBDs and remote DBDs.

treatments. The substrate is located between the two planar electrodes similar to low-pressure plasma tools. Fig. 1(b) is a surface-barrier DBD with coplanar electrodes in which the plasma is generated between the two electrodes. The substrate is located above the coplanar DBD source and the area facing the electrode is treated by the plasma. A remote DBD is also investigated to prevent plasma-induced damage during plasma exposure and to produce radicals by gas dissociation; an example type is shown in Fig. 1(c) [9]. There are numerous variations of these DBD sources, some of which are shown in Fig. 1(d) to (f). By using a multi-pin shaped, instead of a planar, electrode as the power electrode, a higher plasma density was obtained for the simple parallel plate DBD source and the remote DBD source shown in Fig. 1(d) and (e), respectively, due to the concentration of the electric field near the tip area [10–12]. A double-discharge system composed of direct DBDs and remote DBDs was also investigated to improve the plasma density and gas dissociation, and to provide ion bombardment at the substrate [13,14].

In all DBD systems, the accumulated surface charge on dielectric barriers must be neutralized, e.g., by AC power or bipolar pulsed DC power in either static or flowing gas regimes. Due to the accumulated charge on dielectric barriers, a uniform glow discharge plasma regime is obtained at low operating voltages. From the viewpoint of plasma generation method and scalability, the DBD method, which provides non-thermal uniform glow-type plasma conditions, is one of the most popular approaches for flexible and printed electronic devices [5,7,15,16]

2.2. Atmospheric pressure plasma jets and plasma torches

Fig. 2 shows a schematic diagram and an image of an atmospheric-pressure plasma jet (APPJ) which can be operated with radio frequency (RF) power or microwave power.[17] The ionized gas from the plasma jet flows out through a nozzle, where it is directed onto a substrate, located a few millimeters to a few cm downstream. This APPJ source configuration has been used for many applications including the surface treatment of variety of materials and biomedical applications including the induction of apoptosis in cancer cells [6,18–23].

The APP torch system shown in Fig. 3 has similar characteristics to APPJs except that the plasma is generated between the tip of the center electrode and the ground electrode near the exit of the torch.[24] Many researchers have employed plasma torches for materials processing, including silicon etching [6,25], photoresist ashing [26], and deposition of SiO_x or TiO_x films [27–30]. APPJs are characterized by relatively low electron and gas temperatures, because gas molecules are dissociated between the electrodes in a glow micro-discharge. In the case of plasma torches, a very high voltage of 10 to 50 kV is generally applied, and the reactive gas is dissociated in an arc discharge. Therefore, a typical atmospheric-pressure plasma torch tends to have significantly higher gas temperature and plasma density found in APPJs. [6,31]

2.3. Corona discharges

A corona discharge is defined as a luminous glow localized in space around a sharp tip in a highly non-uniform electric field. Corona discharges are electrical discharges formed by ionization of a gas surrounding a conductor; this occurs when the potential gradient at the sharp tip exceeds a certain value but is not sufficient to cause complete electrical breakdown or arcing [32–34]. By applying a high voltage to the sharp electrode, small localized discharges can be observed in the gas gap of about 1 to 10 mm. Schematic diagrams of corona discharge systems are shown in Fig. 4 [17,35]. The systems consist of (a) a pencil-like metallic pin or (b) multiple metallic pins attached to a metallic power electrode and a ground electrode. There is no dielectric plate between the electrodes limiting the current. If a non-electronegative gas such as He or Ar is used as the supply gas instead of air, the discharge is enhanced and can be operated at a relatively low voltage. The pin array is biased by a DC, AC, or pulsed power supply. In the drift region outside this volume, charged species diffuse toward the planar electrode and are collected. Corona discharges in air are commonly used for ozone

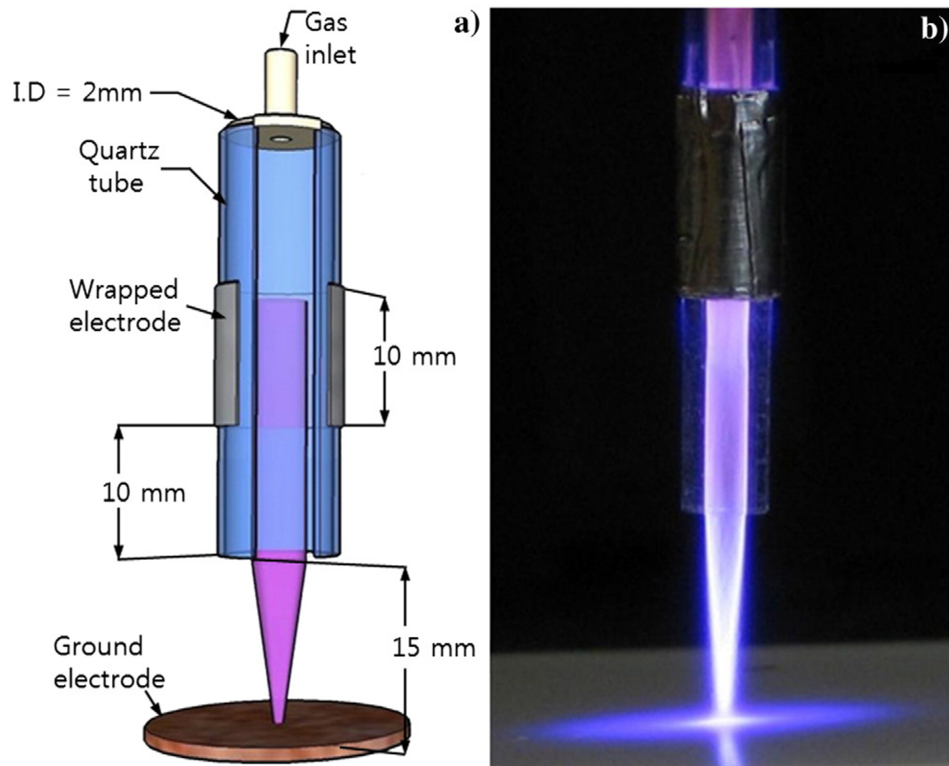

Fig. 2. (a) schematic drawing showing the structure of an APP jet electrode unit and (b) an image of an atmospheric plasma jet operated with a 5-slm helium flow and 1 W input power [17].

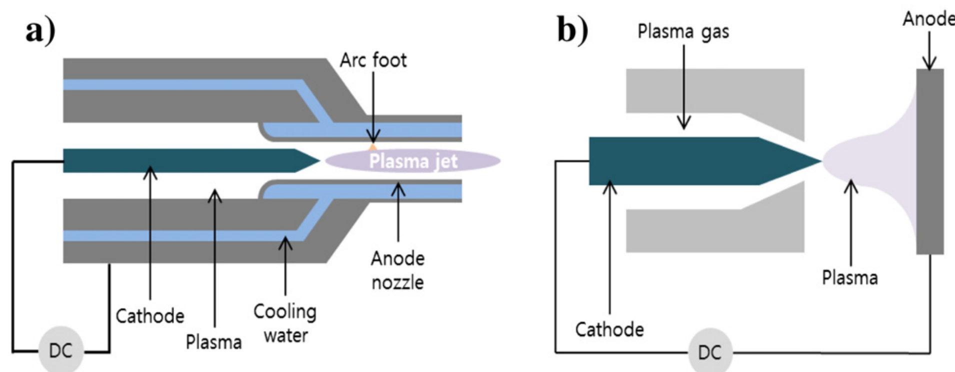

Fig. 3. Schematic drawings of atmospheric-pressure plasma torches which have (a) coaxial electrodes and (b) non-coaxial electrodes. In the plasma torch, the plasma is generated between the tip of the center electrode and the ground electrode near the exit of the torch [24].

production [36] or for the activation of polymer surfaces before printing, pasting, or coating [37,38].

Despite many advantages, there are some issues to be investigated further. These are arc, streamers, etc. resulting from a typical feature of atmospheric discharges at high voltages between electrodes separated by more than few millimeters [3]. This makes the plasma strongly non-uniform and not desirable for the surface treatment of some of materials such as soft materials because of damage from the arcs and streamers [3–5]. Prior to applying the APP process to flexible and printed electronic devices, a thorough optimization of driving frequency, gas flow rate, special electrode shape, etc. should be accomplished.

3. APP applications for flexible and printed electronics devices

As mentioned above, APP is attractive for both economic and technological reasons. Potential cost saving factors are associated with the in-line processing capability in addition to avoiding the use of expensive vacuum related components, which substantially reduces the substrate handling costs, and leads to an increased throughput. APP technology could be an especially powerful, industrial alternative for processing of flexible and printed electronic devices because of simplicity without vacuum, scalability, high process speed, etc. We will focus on topics such as surface treatment and activation, surface etching and texturing, sintering, and deposition related to the flexible and printed electronic devices.

3.1. Surface treatment and activation

Surface treatment and activation using APP is of great interest for flexible substrates and printed electronics. A brief review of a few research studies demonstrating the potential prospects of APP sources and their findings is discussed below.

Flexible organic solar cells (OSCs) have been intensively investigated as the next generation solar cell due to their light weight, robust profile, superior flexibility, low cost, and continuous fabrication process based on roll-to-roll coating. Owing to the advantages of low resistance, high transmittance, and superior flexibility, amorphous ZnO-doped In_2O_3 (IZO) or IZO–Ag–IZO electrodes grown by roll-to-roll sputtering have been employed as flexible transparent electrodes in flexible OSCs. After the sputter deposition of the IZO anode layer, the development of a cost-effective and low-damage surface cleaning process for the flexible anode is very important because the adhesion between the IZO and the poly (3, 4-ethylenedioxythiophene): poly (styrenesulfonate) (PEDOT: PSS) layer deposited on the IZO layer is critically influenced by the surface cleaning method.

In an experimental study carried out by Park et al., using a remote DBD linear in-line atmospheric plasma system shown schematically in Fig. 5, a flexible IZO electrode was treated using an Ar/O_2 plasma to investigate the effect of APP treatment on the electrical and optical properties by measuring contact angle, surface energy, sheet resistance, and transmittance [39]. The results are shown in Fig. 6(a) for contact angle and surface energy and (b) for sheet resistance and optical transmittance as a function of rf power to the APP source. As shown in Fig. 6(a), a reduction in the contact angle from ~68 to ~0° and a significant enhancement in the surface energy has been observed by an applying rf power of 100 W to the flexible IZO substrate. This is due to effective removal of organic residues and contaminants from the IZO surface formed during the storage of the IZO substrate in the air. In addition, as shown in Fig. 6(b), the surface treatment did not change the sheet resistance and optical transmittance of the flexible IZO surface noticeably, indicating no damage effect on electrical and optical properties of the IZO during the plasma surface treatment.

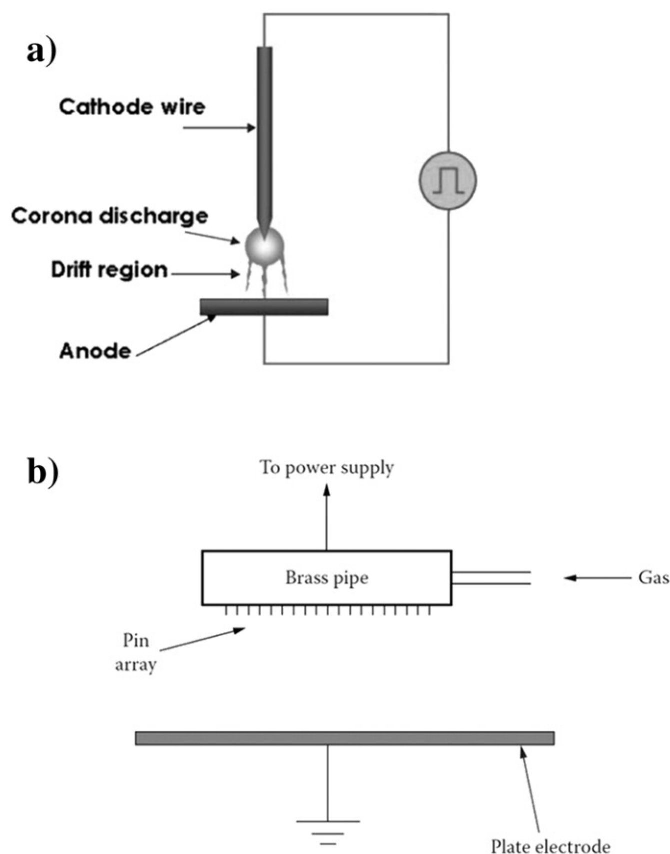

Fig. 4. A corona discharge system consisting of (a) a pencil-like or (b) multiple metallic pins attached to a metallic power electrode and a ground electrode. There is no dielectric plate between the electrodes limiting the current [24,35].

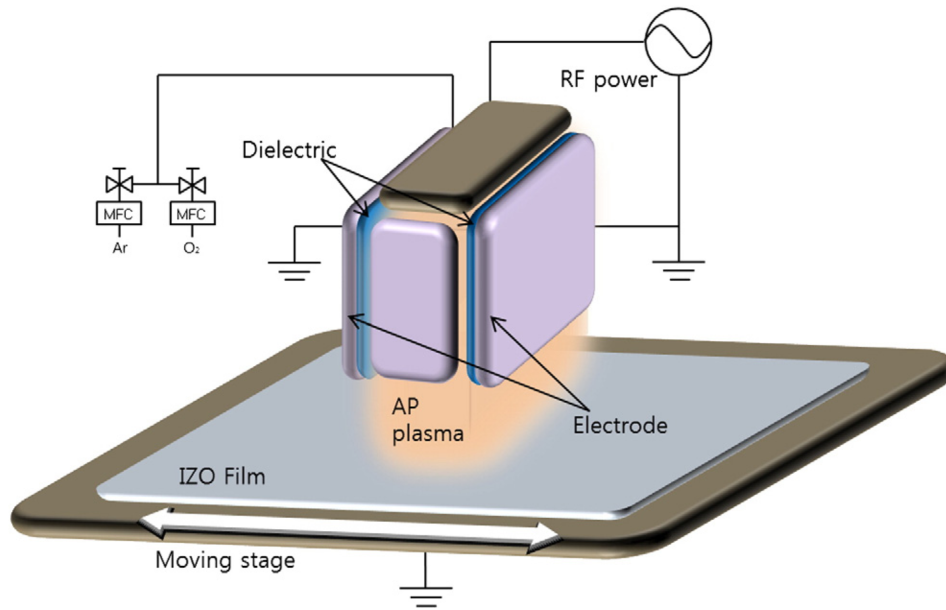

Fig. 5. Schematic of a remote DBD linear in-line plasma treatment system [39].

ZnO has a great potential for a variety optoelectronic applications in the ultraviolet (UV) region due to its wide band-gap of 3.37 eV, large exciton binding energy of 60 meV, and the availability of large-area ZnO substrates [40,41]. Furthermore, ZnO thin films are investigated as a promising engineering material for the fabrication of transparent thin film transistors (TTFTs) on glass or plastic substrates [42,43]. Owing to its wide applications, ZnO has attracted serious research interest in the last several years. Jung et al. [44] carried out a study to investigate the effect of atmospheric rf plasma treatment of plastic (polycarbonate; PC) substrates on the properties of ZnO thin films. PC substrates were treated by Ar/O_2 plasmas by varying the gas ratios. The ratio of Ar and O_2 (O_2/(Ar + O_2)) has been varied from 0 to 1. Then, the ZnO films were deposited on those substrates treated by the atmospheric plasmas. Fig. 7 shows characteristic X-ray spectra of ZnO deposited on the plastic substrates treated by the APP with varying O_2 ratio. The strong peaks in the range of 34.15 to 34.22° (2θ) correspond to the (002) Bragg peaks of wurtzite ZnO with the c-axis preferentially oriented perpendicular to the substrate as shown in Fig. 7. This suggests that ZnO samples with a fine polycrystalline structure have been fabricated. The intensity of the diffraction peaks is minimum at an O_2 fraction of 0.3. The full-width-

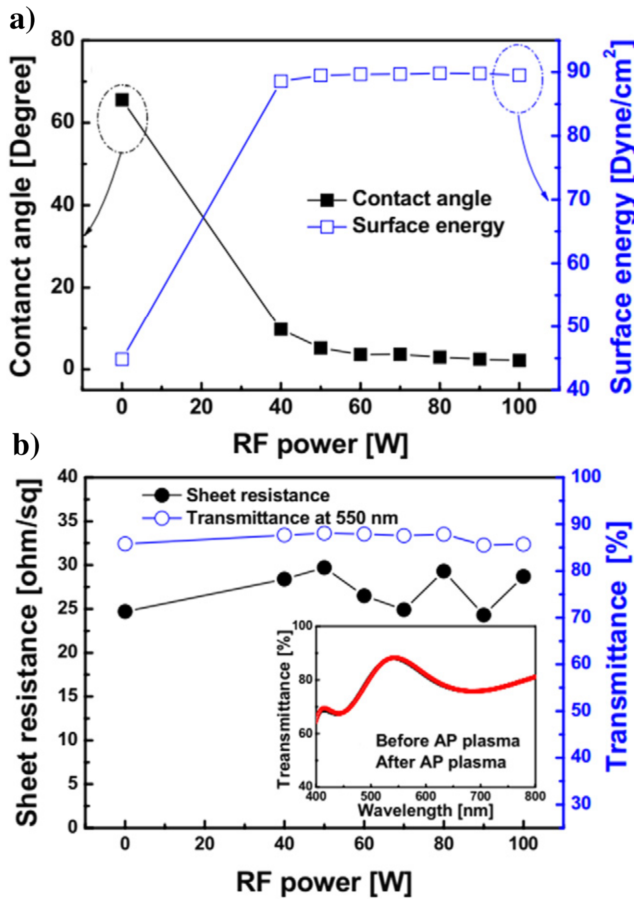

Fig. 6. (a) plot of contact angle and surface energy of APP-treated IZO electrodes as a function of the rf power. (b) plot of sheet resistance and optical transparency (550 nm) as a function of the rf power to the APP source. The inset shows the optical transparency of the untreated and APP treated IZO electrodes indicating no changes after the treatment [39].

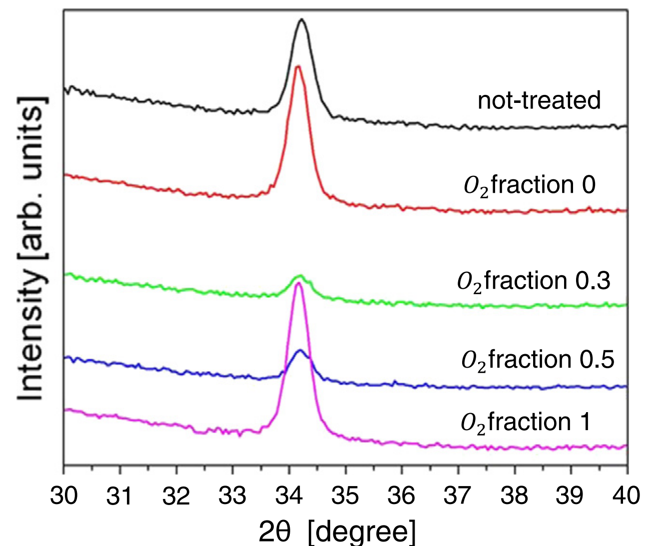

Fig. 7. Characteristic X-ray scams from ZnO films grown on PC substrates treated by APP as a function of O_2 fraction in O_2/(Ar + O_2) [44].

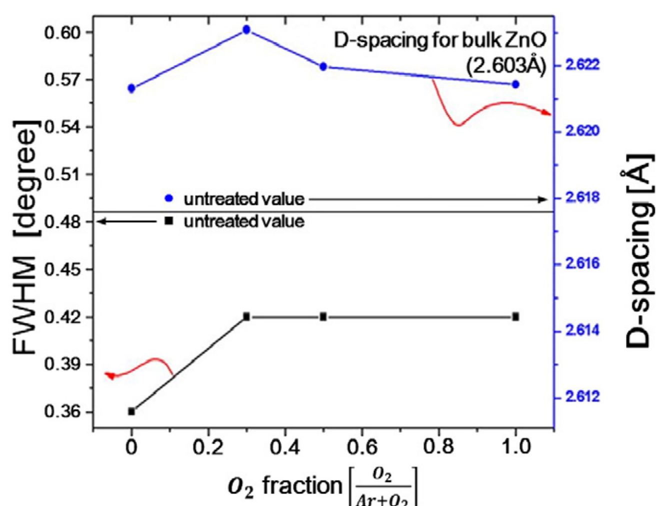

Fig. 8. FWHM and d-spacing of ZnO films grown on PC substrates treated by APP for 5 min as a function of O_2 fraction $O_2/(Ar + O_2)$ [44].

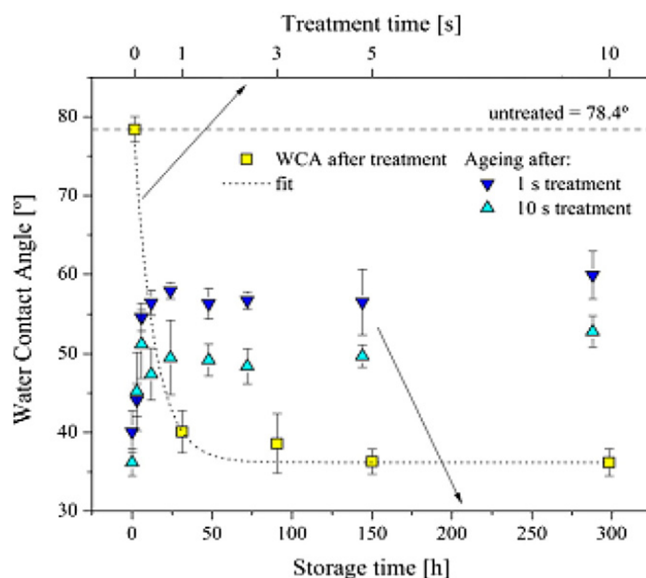

Fig. 10. Water contact angle measurements of DCSBD-treated PET surfaces as function of plasma treatment time and storage time [45].

half-maximum (FWHM) of the Bragg peak (002) and the d-spacing of as-grown ZnO films are shown in Fig. 8. The increasing FWHM and d-spacing values indicate a decrease in the average crystalline size and compressive stress in the films, respectively. The FWHM and d-spacing increase with increasing O_2 ratio of 0.3, and then decrease. It shows that the plasma treatment apparently brought about a higher compressive stress, as evidenced by d-spacing values, which were larger than those for untreated samples. The results, shown in Figs. 7 and 8, suggest that the best ZnO crystal structure with the largest average grain size has been achieved on the PC substrates treated in the pure argon plasma. However, it was observed that a ratio of O_2 less than 0.3 is generally necessary to obtain ZnO films having good structural quality. The authors believe that the variation of the ZnO crystal structure deposited on the PC substrates treated by the APP as a function of O_2 ratio in Ar/O_2 is related to the formation of –OH radicals binding to the PC surface and the presence of –OH on the PC surface treated by the plasma induces better ZnO crystallinity.

Homola et al. [45] reported the effects of atmospheric plasma treatments on the properties of polyethylene terephthalate (PET) surfaces. The APP was generated using a diffuse coplanar surface barrier discharge (DCSBD) in ambient air, as illustrated in Fig. 9. The variations in wettability, surfaces roughness, and surface energy of PET surfaces were studied. The water contact angle of PET surface measured as a function of plasma treatment time and with storage time after the treatment for different DCSBD plasma treatment times are shown in Fig. 10. As shown, after 10 s of plasma treatment, the water contact was reduced from 78.4 to 36.2°. Prolonging the plasma treatment time showed only minimal effect on water contact angle and surface energy. The plot of surface energy variation with plasma treatment time is shown in Fig. 11 and it is observed that the surface energy is increased from 50.6 to 73.8 mJ m^{-2} after a plasma treatment of 10 s. Since the water contact angle and surface energy are related to wettability, therefore, from Figs. 10 and 11, it is apparent that the highest change in wettability, i.e., change of water contact angle and surface energy has been achieved after the plasma treatment of 1 s.

Using a remote pin-to-plate type DBD source (shown in Fig. 1(e)), Park et al. carried out an experimental study to investigate the effect of $N_2/He/SF_6/O_2$ plasma treatment on the water contact angle and adhesion of Ag/Cu deposited on polyamide (PI) films; the results are shown in Fig. 12 [10]. The discharge was initiated with pulsed AC power of frequency 60 kHz and a duty cycle of 50%. They used the pulsed AC power to improve the stability of the discharge and to suppress filamentary discharges. Regarding gas composition, the flow rates of N_2 (40 slm)/He (1 slm) used as the carrier gas were fixed and the flow rates of SF_6 and O_2 were varied. The use of SF_6 (1.2 slm)/O_2 (0 slm) in the gas mixture increased the contact angle and showed a large C–F bonding percentage on the PI surface while the use of SF_6 (0 slm)/O_2 (0–2 slm) decreased the contact angle and showed high C=O bonding. The C=O bonding is related to the adhesion of materials deposited on the PI surface; therefore, the increase of C=O bonding percentage on the PI surface increases the adhesion strength. Initially, the increased C=O bonding percentage on the PI surface can be obtained by increasing

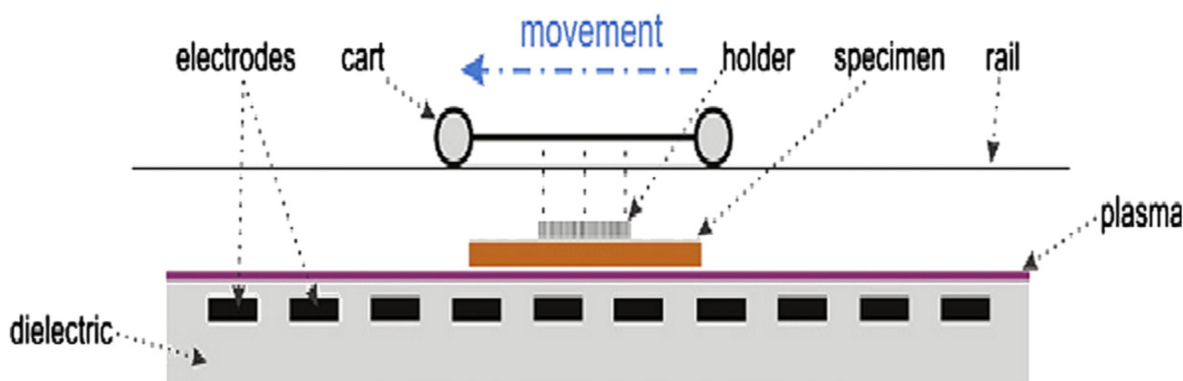

Fig. 9. Experimental set-up of a diffuse coplanar surface barrier discharge (DCSBD) for plasma treatment of PET surfaces [45].

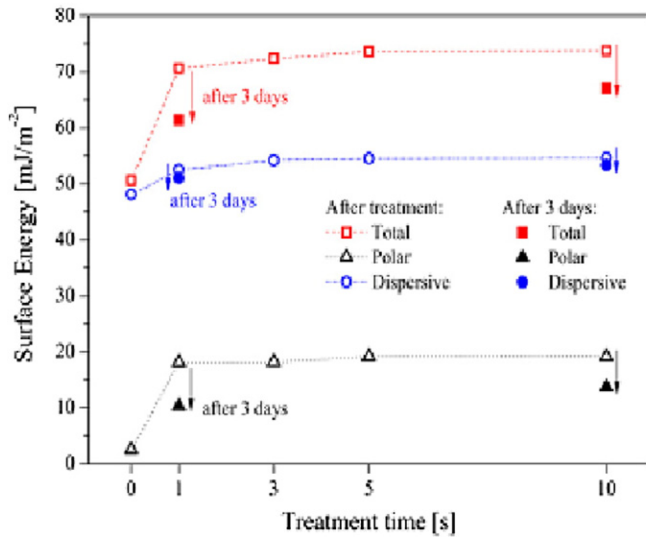

Fig. 11. A plot of surface energy as a function of plasma treatment time for DCSBD treated PET surfaces [45].

the O_2 flow rate in the gas mixture; however, when the O_2 flow rate was higher than a certain value, due to the formation of a filamentary discharge, the plasma density and the C═O bonding percentage decreased. In contrast, when SF_6 (1.2 slm) was added to O_2 (0.9 slm), the stability of the plasma was increased without forming a filamentary discharge and the higher plasma density could be obtained. Therefore, with the gas mixture of $N_2/He/SF_6/O_2$, not only the lowest contact angle (9.3°), but also the highest C═O bonding percentage on the plasma treated PI surface was obtained. Also, when Ag (10 nm)/Cu (10 μm) was deposited on the PI films with/without the plasma treatment, as shown in Fig. 12(c), the Ag/Cu deposited on the plasma treated PI had an adhesion strength three times higher than that deposited on untreated PI.

Fleischman et al. [46] investigated the effect of helium–oxygen (He–O_2) and helium–water vapor (He + H_2O) plasmas at atmospheric pressure on the surface properties of polyethylene naphthalate (PEN) films: wettability, chemical functionalization, and surface energy. In addition, the influence of the atmospheric plasma treatment of the PEN film on the morphology and quality of inkjet-printed lines of poly (3,4-ethylenedioxythiophene) poly(styrenesulfonate) (PEDOT:PSS) dispersed in an aqueous solution was also investigated. For this experimental study, a commercially available roll-to-to-roll DBD type plasma system, as shown in Fig. 13, has been used. In this system, the cylindrical ground electrode covered with a dielectric material of Al_2O_3 was rotated to serve as the roller in the hybrid roll-to-roll process capable of throughputs of up to 5 m/min. Two aluminum high-voltage electrodes were positioned above the roller, at a distance of 2 mm, and had slit channels to allow gas diffusion.

The inkjet printing studies of PEDOT: POS have been carried out on three different PEN samples: (1) as received, (2) He + O_2 (0.5% of oxygen in helium, 0.94 W/cm^2 power density, and a plasma exposure time of 13.5 s, and (3) He + H_2O (1.04 W/cm^2 power density and a plasma exposure time of 6.75 s). These conditions were chosen on the basis of the lowest water contact angle and the maximum surface energy. Fig. 14 shows optical microscope images of inkjet-printed PEDOT:PSS lines as a function of PEDOT:PSS ink spacing between the centers of two consecutive ink droplets for the above three samples. The droplet spacing on line deposition for each of the different plasma treated PEN substrates was varied from 25 to 125% by changing the centers of two consecutive droplets from 25% to 125% of the measured in-flight droplet diameter of 80 μm. Due to a high water contact angle, the as-received PEN samples exhibited discontinuous lines composed of isolated PEDOT:PSS droplets. The size of droplets increases with increasing spacing between two adjacent droplets as shown in Fig. 14(a). However, due

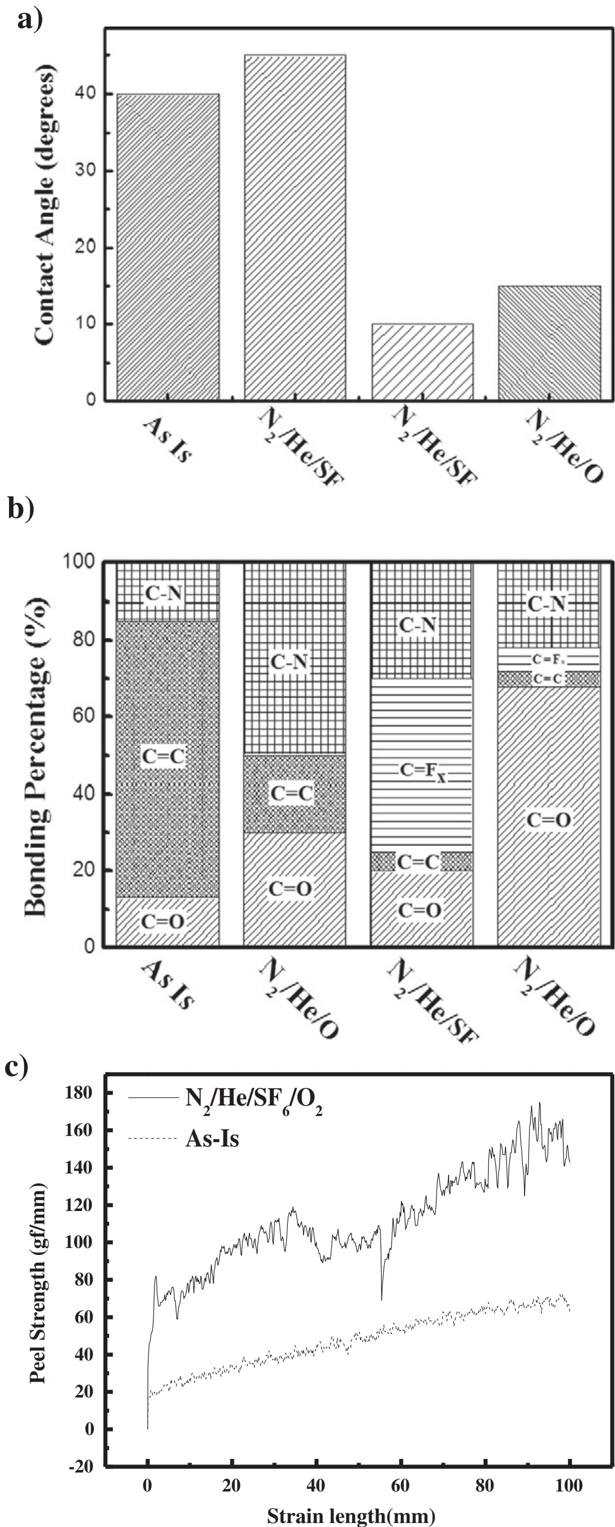

Fig. 12. (a) water contact angle of PI films after APP treatments with various gas mixtures, (b) chemical bonding percentage of carbon on the PI film surface after the plasma treatments, and (c) 180 degree peel strength of Ag (10 nm)/Cu (10 μm) on the PI substrate deposited with/without plasma treatment of the PI substrate surface using $N_2/He/SF_6/O_2$ [10].

to a lower water contact angle, the PEN samples treated with (b) He + O_2 and (c) He + H_2O plasmas show large liquid instability at small droplet spacings. This instability is reduced and a stable line is formed with increasing droplet spacing. If the droplet spacing becomes too large, the uniform line becomes distorted with a scalloped shape.

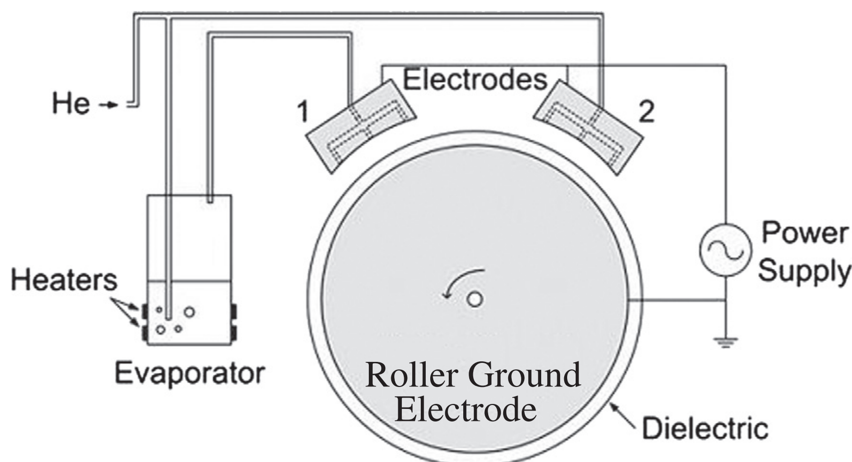

Fig. 13. Schematic of the experimental set-up used to treat PEN substrates by roll-to-roll processing using APP with gas mixtures of He/O_2 and He/H_2O [46].

These experiments reveal the potential of APP for inkjet printing on flexible substrates.

Many more studies [47–51] have been carried out using various DBD type atmospheric plasmas to investigate the treatment effects on flexible substrates and for enhanced understanding of kinetics, mechanisms, and maneuvering of such plasma sources to achieve the desired results. All these studies reveal the potential of atmospheric plasmas for the surface modification of plastic substrates.

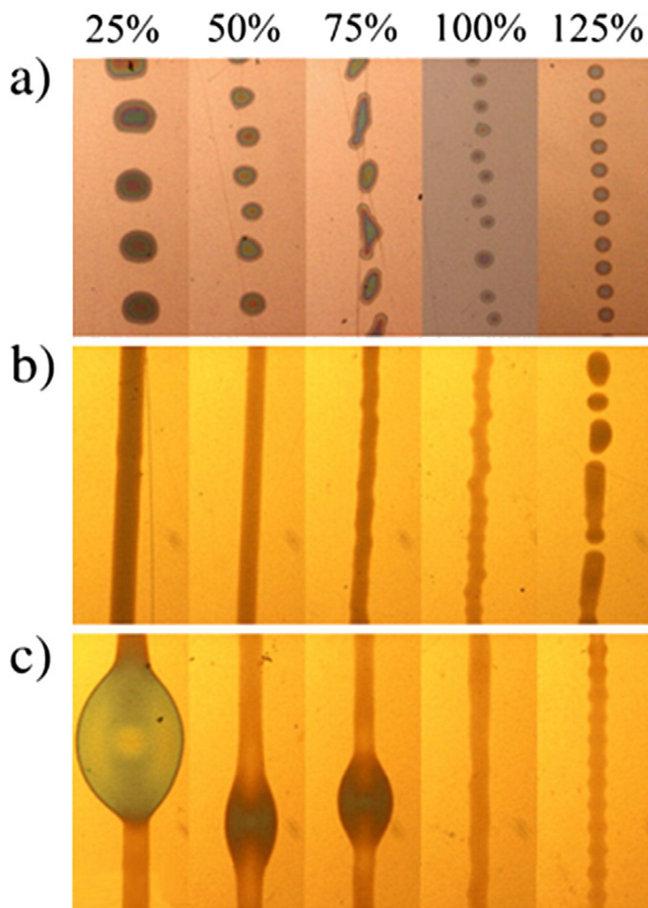

Fig. 14. Optical microscopic images of inkjet-printed PEDOT:PSS lines as a function of PEDOT:PSS ink spacing (25–125%) on (a) as-received PEN, (b) He/O_2 plasma treated PEN, and (c) He/H_2O plasma treated PEN [46].

3.2. Surface etching and texturing

The application of a direct writing processes such as inkjet printing to microelectronic processing has many advantages, including low cost, no material waste, easier control of pattern shape, etc., compared to conventional lithographic methods. Therefore, the inkjet printing process is considered to be one of the next generation microelectronic processing technologies that can be applied to flat panel displays. In addition, inkjet printing is a potential low-temperature process that may enable manufacturing on flexible substrates. Also, it is compatible with continuous roll-to-roll processing and scales more favorably with increasing substrate area than lithographic processes.

Controlling pattern size is a highly critical issue for the application of inkjet printing to industrial manufacturing processes, especially for metal inkjet processing such as Ag, Cu, etc. and it depends on surface-wetting properties. For the inkjet printing process, it is necessary to have a hydrophobic surface in order to obtain a fine line pattern and, at the same time, a hydrophilic surface to provide improved adhesion. One of the techniques to provide a hydrophobic surface with improved adhesion is to increase the surface area contacting the ink by forming microscopic texturing on the substrate surface. APPs with micro-masking and selective etching processes have been used as a potential tool for microscopic texturing on a variety of substrates, including polymers for roll-to-roll processing, to increase ink adhesion, to enhance the light collection efficiency of solar cells, etc. [11,12,52,53].

Using in-line-type APPs, J. Park et al. [11] have performed an experimental study to achieve fine microscopic texturing on polyimide (PI) films, which have a pyromellitic dianhydride-oxydianiline (PDMA-ODA) structure, for direct inkjet printing. The experimental in-line plasma source set-up is shown in Fig. 1(f) and is composed of two remote plasmas on the topside for reactive gas dissociation and one direct DBD on the bottom side of the source for selective etching. For the generation of remote plasmas, 30 kHz AC power was applied to the two side copper electrodes while the top center electrode is grounded. The bottom electrode, on which the substrate is located, was grounded or connected to a quasi-pulse power supply with a frequency of 60 kHz to generate an additional direct plasma. All of the electrodes were covered with a 2 mm thick Al_2O_3 plate.

The texturing process of PI films consisted of two steps: (1) hexamethyldisilazane (HMDS) deposition/oxidation using the remote plasmas for micromasking and (2) selective etching of PI and mask removal using combined remote /direct combined plasmas as shown in Fig. 1(f). During the first step, to deposit a thin silicon oxide mask layer on the polyimide film, a (HMDS)/He/O_2 gas mixture for the deposition of the mask layer and a He/O_2 gas mixture for its

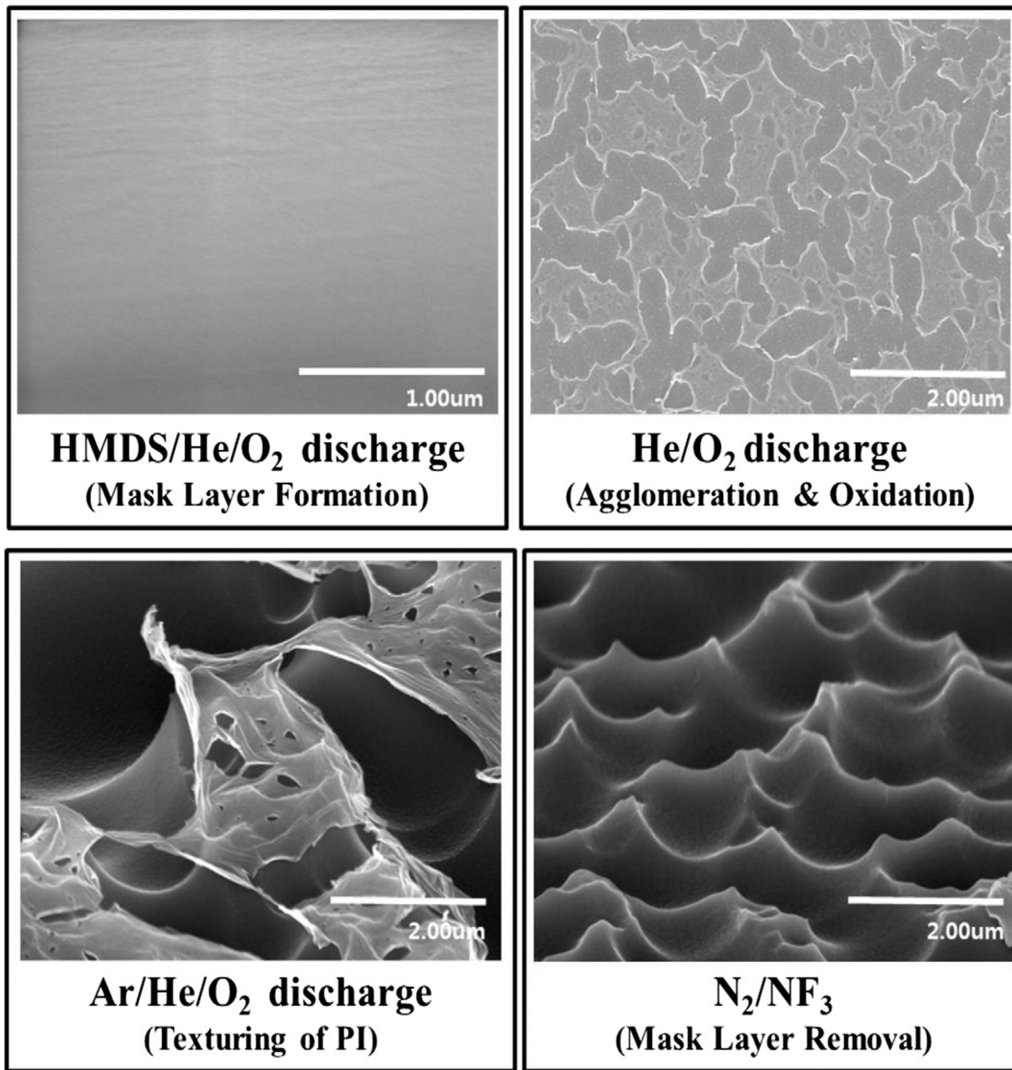

Fig. 15. Surface images of polyimide films, obtained by field emission scanning electron microscopy (FE-SEM), after treatment using atmospheric plasmas. The images are after the HMDS deposition, agglomeration and oxidation, selective polyimide etching, and SiO_2 mask removal [11].

agglomeration and oxidation have been used. During the second step, a $He/O_2/Ar$ gas mixture for the selective etching of the polyimide surface and an N_2/NF_3 gas mixture for the removal of the mask layer were used. The surface morphologies of PI during the texturing step are shown in Fig. 15. After removal of the SiO_2 mask layer using a N_2/NF_3 plasma, a textured surface composed of trenches about 2 μm wide and 0.5 μm deep was formed. After the texturing, the contact angle increased from 33.4°(as is) to 105.7° (textured) indicating the increased hydrophobicity of the textured PI surface. Ag ink dots were printed on both "as is" and textured PI films and the Ag dot pattern widths were

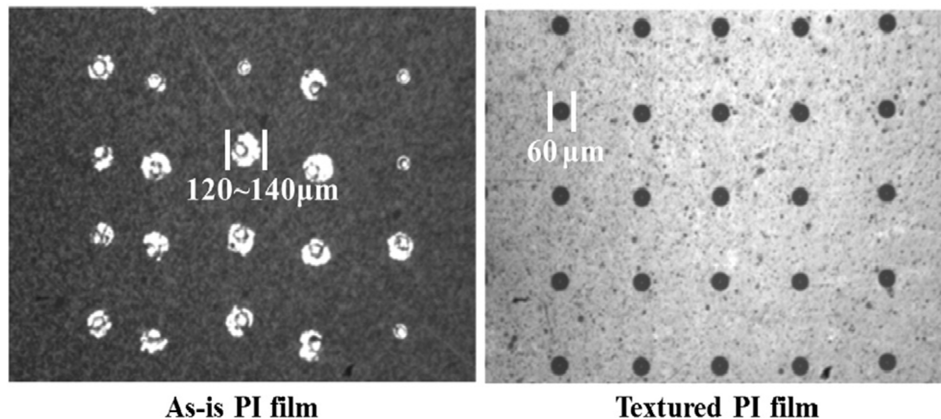

Fig. 16. Optical microscope images of polymer films with metal patterns, Ag metal dot patterns are formed by inkjet printing system on (a) an as-is polymer film and (b) an APP textured polymer film (see text for details) [11].

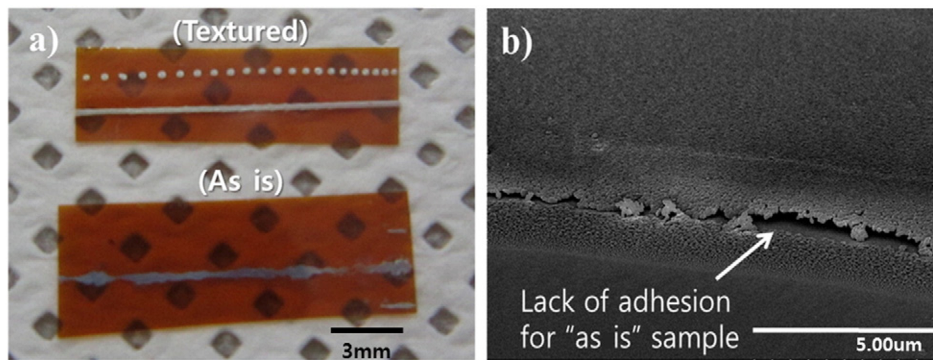

Fig. 17. (a) Photographs of a polymer film patterned with Ag metal dots and lines using inkjet printing followed by a tape peel test for comparing the adhesion force on the as-is and the textured regions of the film. (b) SEM image of Ag metal patterned on an as-is PI surface showing the lack of adhesion between Ag ink and PI substrate [11].

compared. As shown in Fig. 16, the textured PI film had a more controlled Ag dot pattern width due to increased hydrophobicity on textured PI surfaces. In addition, as shown in Fig. 17(a), when Ag metal dots and lines inkjet printed on the PI films were peeled off using tape, the Ag metal dots and lines printed on the textured PI surface did not peel-off while, those on the "as is" PI surface were partially peeled off. That is, in the case of the textured PI film, the increased adhesion between Ag metal dots and lines and the PI surface was obtained

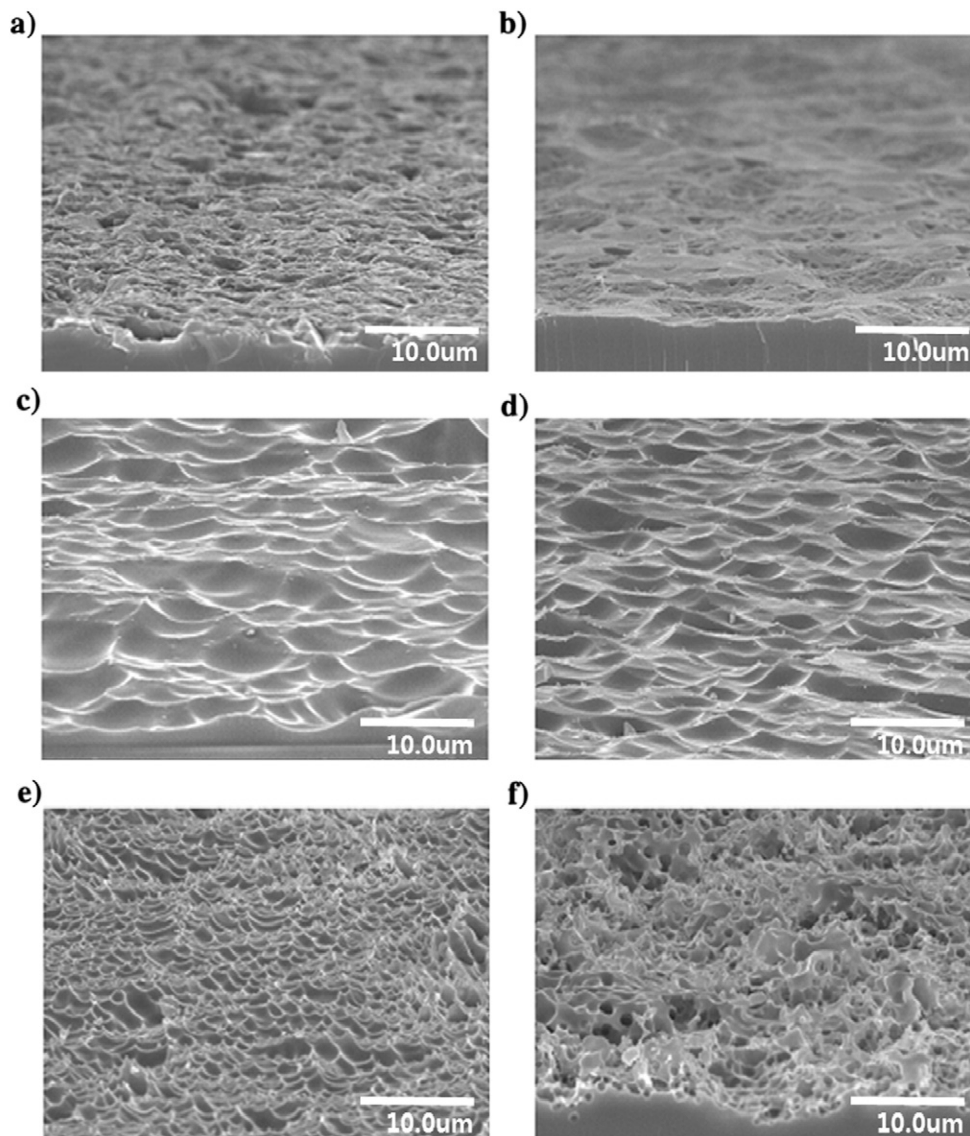

Fig. 18. SEM images of mc-Si surfaces textured using in-line atmospheric pressure plasmas as a function O_2 gas flow rate in N_2 (40 slm)/NF_3 (100 sccm): (a) as-received (sliced mc-Si), (b) 0 sccm, (c) 200 sccm, (d) 400 sccm, (e) 600 sccm, and (f) 800 sccm. The linear substrate velocity was 0.25 m min^{-1} and the substrate temperature was constant at 120 °C [12].

due to the increased contact area while, in the case of the “as is” PI surface, Ag metal dots and lines were detached from the PI film surface due to a lack of adhesion as shown in Fig. 17(b).

Surface etching and texturing using APP has been also applied to other substrates such as multicrystalline silicon (mc-Si) for a decreased light reflection. Microcrystalline (mc)-Si solar cells have been extensively studied for a variety of commercial photovoltaic applications. However, in the process of preparation of mc-Si wafers, the mechanical sawing used to slice the mc-Si ingots results in the formation of macrocracks in the wafers which are detrimental to solar cell efficiency. Therefore, it is necessary to remove mechanical saw damage. Additionally, the front surfaces of mc-Si substrates must be textured in order to increase solar cell efficiency by reducing surface light reflection and increasing the scattering angle for effective light absorption in the bulk absorbed layer. An APP system, such as shown in Fig. 1(e), was used by J. Park et al. [12] to remove the saw damage and texture mc-Si surfaces.

For texturing the sliced mc-Si wafers, N_2 has been used as the discharge gas with NF_3 and O_2 as reactive gasses. Experiments have been carried out to investigate the effect of NF_3 and O_2 on the etching and texturing characteristics of mc-Si wafers and the results are shown in Fig. 18. While the flow rates of N_2 (40 slm) and NF_3 (1000 sccm) were kept fixed, the flow rate of O_2 was varied from 0 to 800 sccm. As shown in Fig. 18(b) and (e), the surface roughness increases with increasing O_2 flow rate. The surface morphology was wavy up to 600 sccm O_2 flow rate and suitable to enhance light trapping at the silicon surface. However, at 800 sccm O_2 flow rate, despite of increasing the surface roughness, the surface morphology becomes irregular which is undesirable for solar cell applications. A plot of surface reflectance in the visible vs. O_2 flow rate is shown in Fig. 19. mc-Si wafer etching without O_2 results in increased reflectance (from 30–40% to 30–60%) due to surface smoothing. However, the surface optical reflectance decreases with increasing O_2 flow rate due to roughening of the surface and is lowest (20–30%) with an O_2 flow rate of 600 sccm. Beyond the 600 sccm O_2 flow rate, the surface roughness increases and becomes more irregular. However, the optical surface reflectance increases indicating that, for lowering the optical reflectance, a wavy surface is preferable to an irregular rough morphology.

In an attempt to maximize light trapping by increasing the optical path length in the absorber layers of a thin film microcrystalline solar cell on glass substrate utilizing $F:SnO_2$ as a transparent conducting electrode and, therefore, to improve the conversion efficiency of the solar cell, J. Hodgkinson et al. [53] introduced a DBD-type atmospheric remote plasma torch for the surface texturing of $F:SnO_2$. Highly-structured $F:SnO_2$ produced by thermal chemical vapor deposition (CVD) was exposed to the afterglow of a remote N_2/HCl plasma torch. The schematic of the DBD remote APP torch used in this study is shown in Fig. 20. A sinusoidal AC voltage of 5–8 kV was applied to generate the visually diffuse glow discharge at atmospheric pressure. Small quantities of hydrogen chloride (HCl) were introduced into the nitrogen flow, which becomes activated in the plasma and helps provide etching of $F:SnO_2$. Atomic force microscopy (AFM) and scanning electron microscopy (SEM) were used to analyze the treated samples. An SEM image of an as-deposited sample is shown in Fig. 21(a). Fig. 21(b) is an SEM image of a sample treated at a voltage of 6.8 kV, a frequency of 2.979 kHz, whereas Fig. 22(c) is from a sample treated at a voltage of 8.3 kV and a frequency of 2.822 kHz. The HCl flow rate, N_2 flow rate, and working distance for both Fig. 21(b) and (c) were the same : 0.3 sccm, 6 slm, and 15 mm. Variations in the size and distribution of the surface features, preferentially removing the smaller peaks, have been observed with varying experimental conditions, as shown in Fig. 21. It has been expected that these etched features will enhance light scattering and thus improve the solar cell efficiency.

Even though the surface texturing techniques described above were not applied for materials texturing on flexible substrates, it is believed that the methods should be applicable to roughening materials deposited on flexible substrates.

3.3. Low temperature plasma sintering

As mentioned in the above section, inkjet printing, using conductive precursor materials like metal nanoparticle inks, has become one of the most important processes in manufacturing contacts and wires for flexible printed electronic devices [54–56]. Generally, metal nanoparticles are dispersed in organic compounds in order to prevent agglomeration in the solvent and to improve processing. [57–60] After inkjet printing using metal nanoparticle ink, the metal nanoparticles are still surrounded by this organic shell, which acts as an insulating layer and prevents electron transfer between the particles. [57] To establish conductivity, conventional heating, [61–64] laser sintering, [65] microwave sintering [66,67] and high temperature plasma sintering [68–70] have been investigated. A general way of establishing conductivity is the thermal sintering method using a temperature above 200 °C. However, this method is not compatible with thermally-sensitive substrates such as polyethylene terephthalate (PET), PI, or PEN used in flexible electronic devices. For that reason, an alternative sintering method through low-temperature

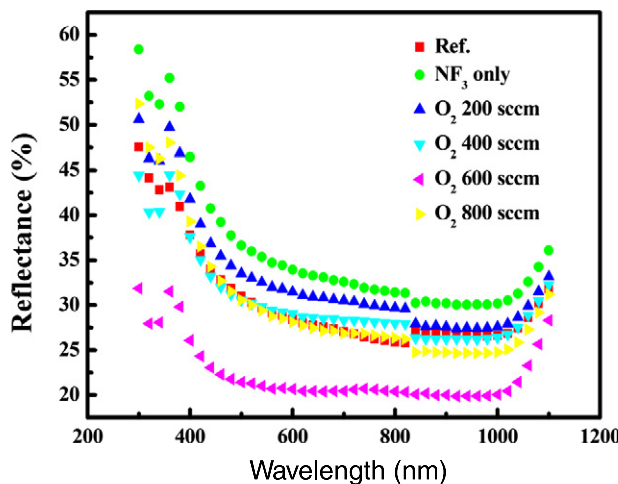

Fig. 19. A plot of the surface visible reflectance of mc-Si textured using an in-line atmospheric pressure plasma as a function of additive O_2 gas flow rate with the N_2 (40 slm)/NF_3 (1000 sccm) [12].

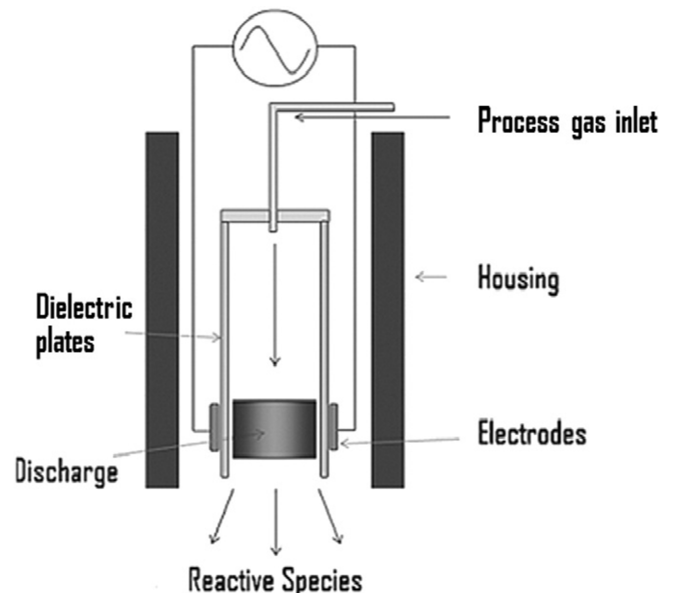

Fig. 20. Schematic of a remote DBD atmospheric pressure plasma torch used to activate the etching process with N_2/HCl. to promote surface texturing [53].

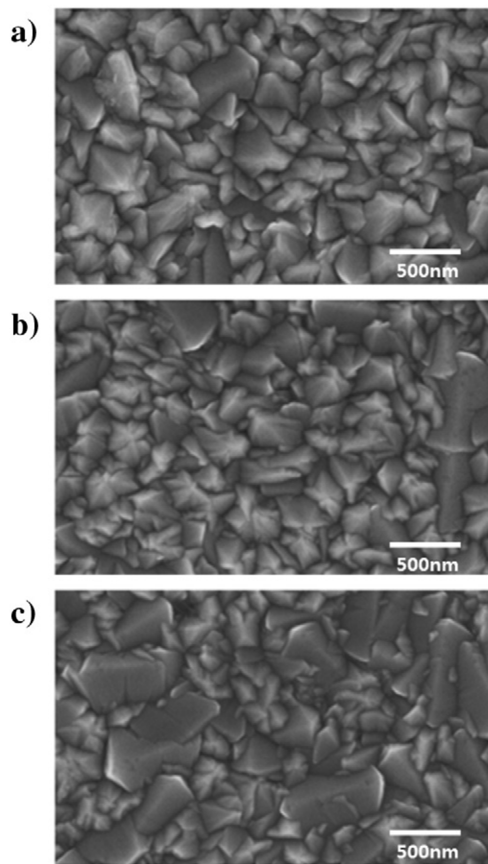

Fig. 21. SEM images showing (a) an as-deposited F:SnO_2 film and (b) and (c) the etched film at different atmospheric pressure plasma surface texturing conditions with N_2/HCl. (see text for details) [53].

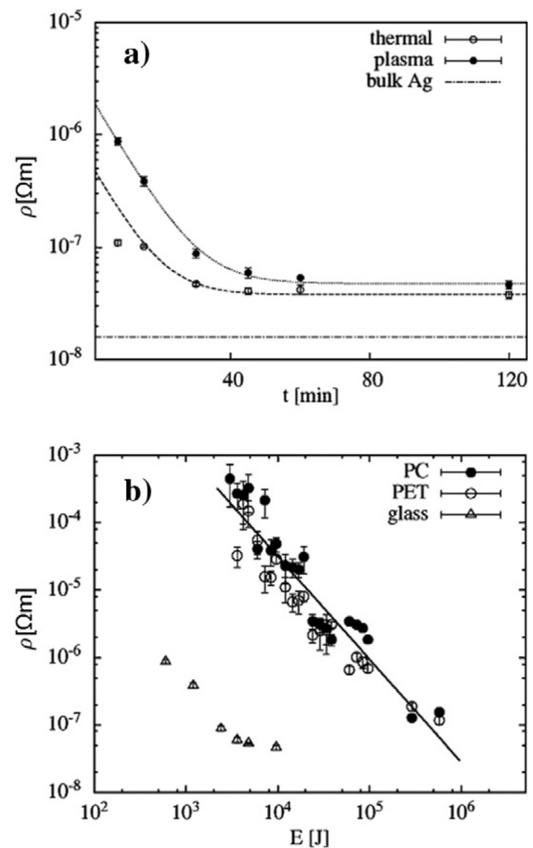

Fig. 22. (a) Resistivity of plasma (80 W) and thermally-sintered inkjet-printed Ag nanoparticle lines on glass. (b) resulting resistivity vs. energy supplied to polycarbonate, polyethylene terephthalate and glass substrates [61].

processing is required for common polymer foils. The search for alternative sintering methods has been focused on plasmas, which are extensively employed in today's manufacturing for various surface treatments. [66–70] Moreover, in the roll-to-roll process for next generation displays, complex vacuum equipment and long sintering times are significant drawbacks for thermal sintering.

Previously, plasma sintering methods have been conducted at low pressure and, by using low-pressure plasma treatments, effects similar to thermal sintering have been obtained. For example, I. Reinhold et al. [61] investigated the effect of low pressure plasma treatments on sintering of inkjet-printed silver tracks. Argon was chosen as the feed gas for plasma generation, since inert gasses did not show noticeable deformation of the polymer substrates. Fig. 22(a) is a plot of the resistivity of Ag tracks on glass substrates as a function of time and sintering method. Thermal sintering was carried out in a convection oven at 220 °C, while 0.75 Torr vacuum and 80 W of 13.56 MHz RF power at room temperature was used for the plasma sintering process. Both methods stimulated solvent evaporation [2,61] and a decrease in resistivity was observed. The results for both polymer and glass substrates (Fig. 22(b)) show an exponential decay in resistivity with increasing energy to the substrate during the plasma sintering. The authors believe that it is caused by the increased ionization of the plasma gas and, as a consequence, the energetic ions as well as ultraviolet (UV) radiation from the plasma decreased the chain length of the organic binding material around the nanoparticles. [55,57,61] The differences in Ag line resistivity between glass and the polymer substrates are believed to be related to the wettability and the thermal conductivity of the substrate which strongly affects sintering. [61] That is, due to the differences in the wettability, the silver line widths on PC and PET were measured to be 169 μm and 218 μm, respectively. The silver line on PET was more effectively sintered than that on PC due to the larger effective surface area for the increased absorption of plasma. The difference in resistivity between glass and polymer substrates was more related to the thermal conductivity of the substrate than the wettability since the line width on glass is smaller despite having the lowest resistivity. In this case, due to the significant differences in the thermal conductivity of the substrates, the substrate temperatures of glass and polymer measured just after the plasma exposure were 81 and 71 °C, respectively.

Fig. 23 shows cross-section SEM images as a function of plasma sintering time for the plasma treatment, 0.75 Torr Ar and 80 W of 13.56 MHz RF power were used at room temperature. [61] Printed silver nanoparticle ink layers were sintered for (I) 7.5, (II) 30, and (III) 60 min at 80 W RF power. In images (I) and (II) images, the sintered and unsintered region could be distinguished. The bottom layer represents the un-sintered nanoparticles, whereas the top layer shows the sintered and conductive material. In image (III), the conductive skin layer has grown to its full extent and the layer thickness decreased due to the densification. [61]

Similar effects have been observed during the plasma sintering at atmospheric pressure. K. Kim et al. [2] measured the electrical resistivity of Cu nanoparticles printed on polyimide substrate as a function of the input energy using DBD (Fig. 24). The sintering process was carried out with oxidation using an Ar/O_2 plasma for decomposition of organic solvent, followed by Cu reduction using an Ar/H_2 plasma while maintaining the substrate temperature at 150 °C. As shown in Fig. 25, the printed patterns sintered at higher plasma powers had lower electrical resistivity than those sintered at low plasma powers. As shown in the insets of Fig. 25, the average cluster size became larger due to inter particle necking caused by volatilization of the organic solvent and decomposition of the dispersants. [2,71–73]

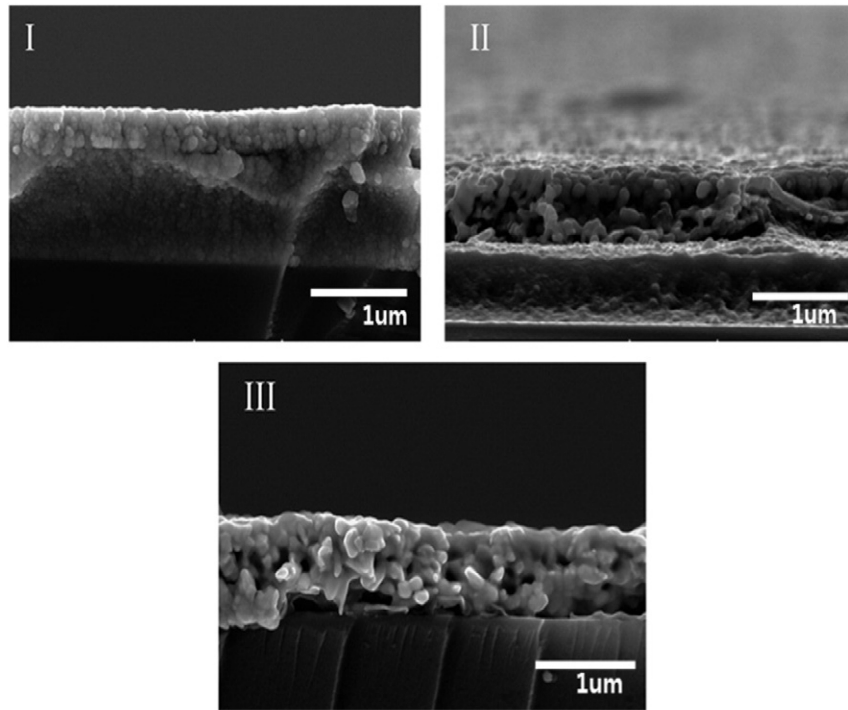

Fig. 23. Cross-sectional SEM images showing the temporal evolution of the sintering process of a silver nanoparticle ink layer on glass after plasma sintering at 80 W for (**I**) 7.5, (**II**) 30 and (**III**) 60 min, respectively [61].

S. Wünscher et al. [57] reported the sintering effect using a pencil-type APPJ on inkjet printed silver nanoparticles on PI substrates. The Ar plasma (4.5 *l*/min Ar flow) was ignited in the plasma pencil by the application of 2 to 6 kV at 1.1 MHz. A photograph of APP system used in sintering process is shown in the upper inset of Fig. 26. As a sintering parameter, the influence of the distance between the printed feature and plasma pencil, referred to as the height (h), was investigated as a function of silver line resistivity by altering the height from 2 to 6 mm while keeping the other parameters constant. Fig. 26 shows that heights of 2 and 4 mm resulted in similar resistivity values of 74.7 and 49.9 μΩcm, respectively. However, sintering at a height of 6 mm yielded resistivities of four to five orders of magnitudes higher. Moreover, a larger scattering of data was observed at 6 mm. The higher resistivity and larger data scattering observed at 6 mm was attributed to the increased oxygen flow to the plasma region as the height between electrode and ground is increased.

Table 1 shows the resistivity results of the inkjet-printed silver nanoparticle ink after different sintering methods including low pressure plasma sintering (using 300 W of a capacitively-coupled argon plasma from Diener Electronics in Germany), APP sintering (using the plasma pencil and plasma conditions shown in Fig. 26), and thermal sintering (at 150 and 230 °C).[57] Three different commercial silver nanoparticle

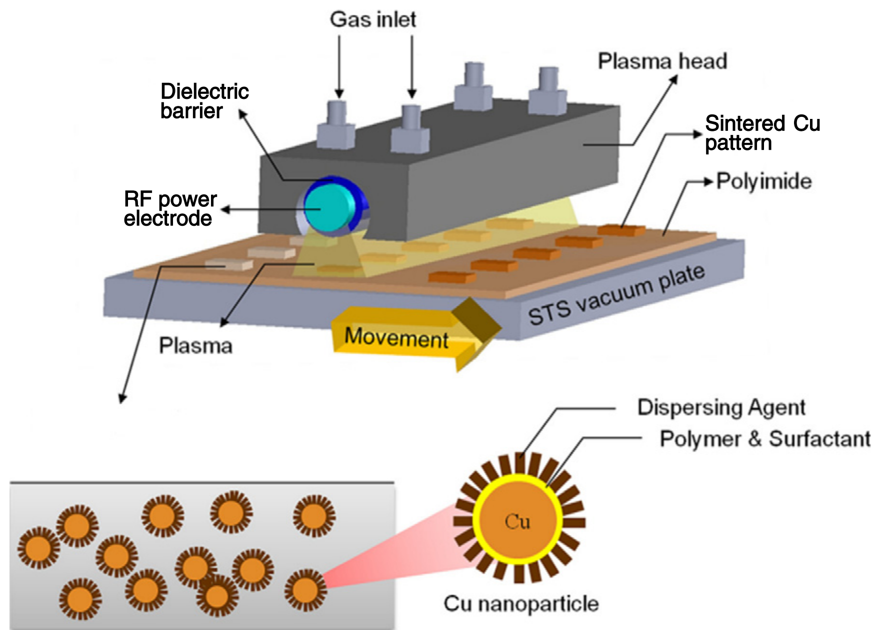

Fig. 24. A remote DBD system used for sintering of screen-printed Cu nano-paste by plasma oxidation and reduction [2].

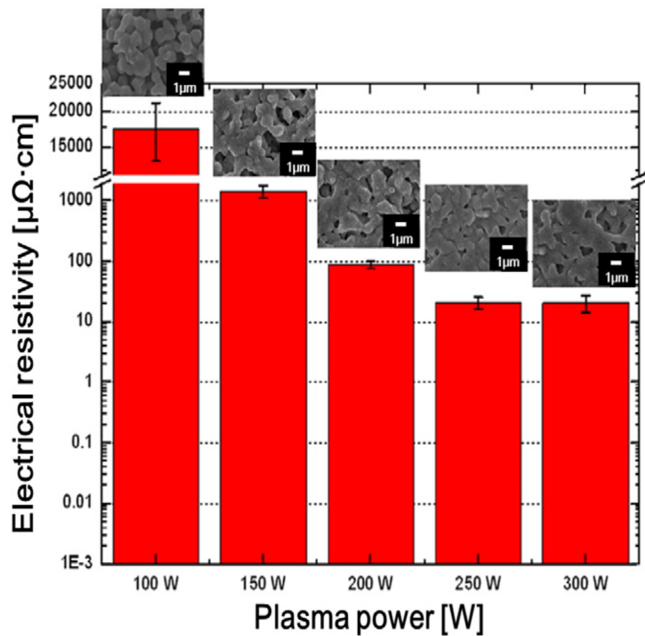

Fig. 25. Electrical resistivity of screen-printed Cu nano-paste sintered by APP as a function of Ar/O_2 plasma power (20 min) for the removal of Cu dispersing-agents/organic-solvents followed by Ar/H_2 plasma treatment (20 min, same power) for Cu reduction. The insets show the SEM images of the Cu nano-paste after the sintering [2].

inks were used. For thermal sintering, the three inks showed significantly different sintering speed and final conductivity, probably due to their different metal loadings, particle sizes, solvent systems and stabilizing agents. Although there are differences among nanoparticle inks, APP sintering shows significantly reduced sintering time of less than 2 min compared to low pressure sintering method, which requires 60 min, to obtain similar resistivity values. Thermal sintering yielded resistivity values of up to one order of magnitude lower than APP sintering.

Table 1
Resistivity (ρ) of three inkjet printed silver nanoparticle inks after argon plasma sintering at atmospheric pressure or low pressure and after thermal sintering for different sintering time [57].

Siliver nano ink sintering methods	Commercial A ink	Commercial B ink	Custom ink
	μΩ · cm	μΩ · cm	μΩ · cm
Atm. pressure plasma (2 min)	16.1	25.4	13.0
Low pressure plasma (2 min)	3.6×10^4	5.0×10^5	207
Low pressure plasma (60 min)	91.5	13.4	15.2
Thermal (2 min)	18.8[a]	Not conductive[b]	Not conductive [a]
Thermal (60 min)	14.0[a]	3.0[b]	4.6[a]

[a] A sintering temperature of 150 °C.
[b] A sintering temperature of 230 °C.

However, as mentioned above, to remove the organic shell, heating of 150 to 230 °C was required for thermal sintering and this is not suitable for thermally-sensitive substrates.

For optimization of the sintering process, S. Wünscher et al. [54] reported the combination of APP sintering and a mild thermal sintering of silver ink containing 20 wt.% of silver nanoparticles on polyethylene naphthalate (PEN) substrate. This method decreased the total sintering time and resistivity significantly and represents an important step toward a roll-to-roll technology. Fig. 27 shows the changes in resistivity as a function of the number of passes at substrate temperatures of 70, 90 and 110 °C. These sintering experiments were carried out with the plasma pencil (kinpen, Neoplas Tools GmbH, Greifswald, Germany) shown in Fig. 26(a) using argon as feed gas at 1.1 MHz and with the RF power less than 20 W. These sintering experiments were carried out at a stand-off distance of 4 mm and a movement speed of 20 mm/s. As shown in Fig. 27, during the APP sintering, more efficient sintering was obtained at the higher substrate temperatures in terms of sintering time as well as resistivity. At 70 °C and 90 °C, the resistivity decreases significantly with the number of passes (that is, with increasing plasma sintering time). However, at 110 °C, the resistivity does not change significantly as the number of passes is increased, showing the lowest resistivity even with a single pass.

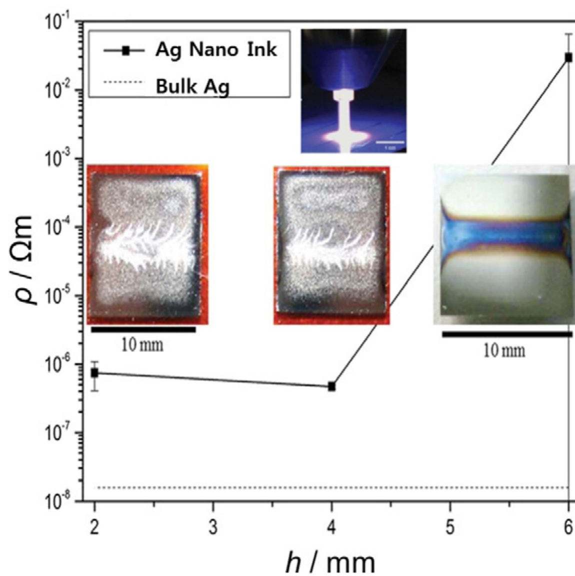

Fig. 26. The influence of the Ar-plasma pencil height (h) on resistivity (ρ) of inkjet printed silver nano-particle on PI substrate after sintering. Silvery appearance of the sintered feature at a height of 2 mm (left inset) and 4 mm (center inset); black appearance of the sintered feature at a height of 6 mm (right inset). The upper inset is a photograph of the plasma pencil [57].

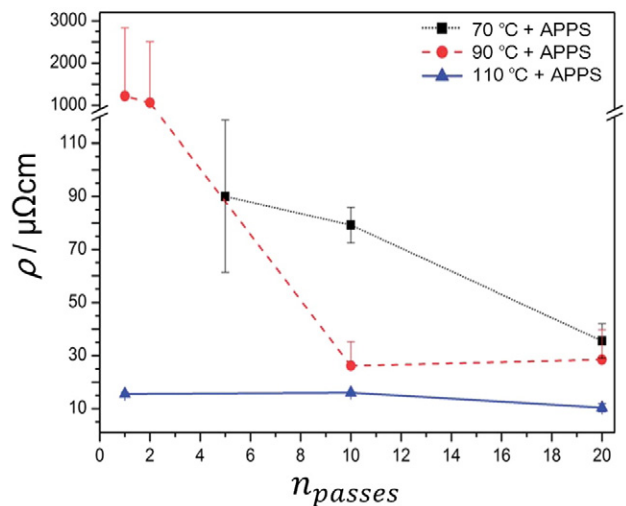

Fig. 27. The resistivity of silver nanoparticle inks on PEN substrates as a function of the number of applied plasma passes and substrate temperature from 70 to 110 °C. These sintering experiments were carried out with the plasma pencil shown in Fig. 26(a) using argon as feed gas at 1.1 MHz and with the RF power of less than 20 W. These sintering experiments were carried out at a stand-off distance of 4 mm and a movement speed of 20 mm/s [54].

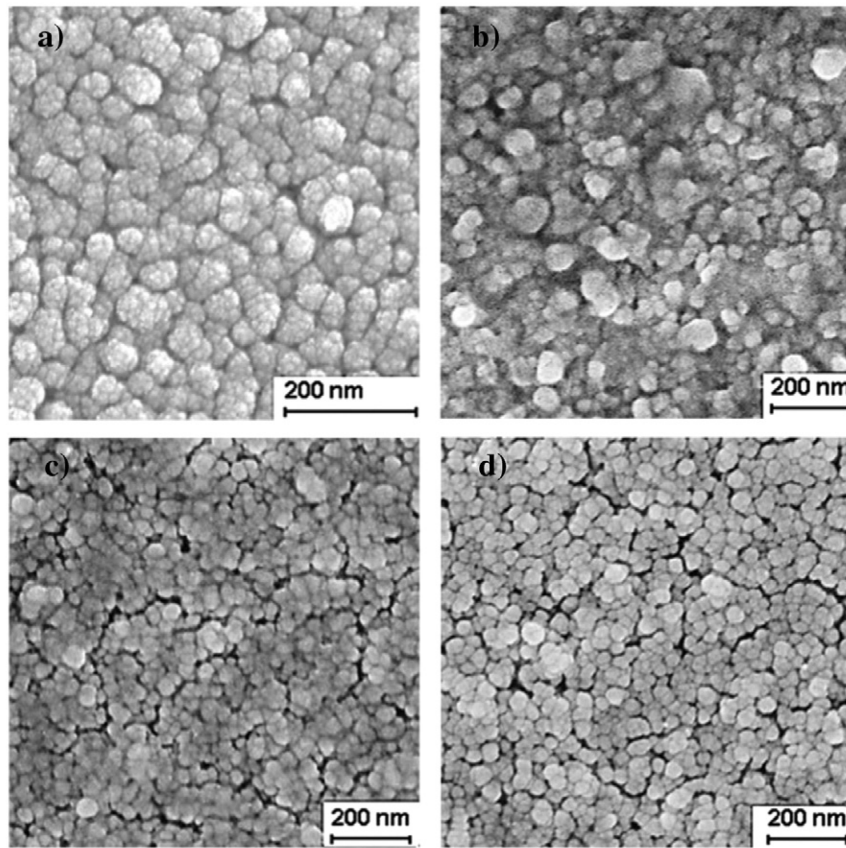

Fig. 28. SEM images of silver nano-particles on PI substrates (a) before sintering and after atmospheric-pressure plasma sintering at 110 °C for (b) 1, (c) 10, and (d) 20 passes [57].

Fig. 28 shows the silver nanoparticle size change from discrete particles before sintering to large silver clusters and a continuous silver network after a single pass of plasma exposure (b) at 110 °C in Fig. 27. The results of multiple passes, 10 and 20, are also shown in Fig. 28(c) and (d), respectively. Before the sintering, particles are discrete with an average size of 50 nm; after a single pass of APP sintering, the silver clusters are larger and form a continuous network. After 10 and 20 passes, a densely-packed silver network is obtained. The combination of elevated substrate temperature and plasma sintering has two effects on the printed silver nanoparticle layer. One is organic solvent evaporation and the other is the promotion of particle coarsening together with increased density of the sintered silver network.

Low temperature plasma sintering of printed electronic materials should be applicable for various applications including ultra-high frequency–radio frequency identification (UHF-RFID) tags, honeycomb

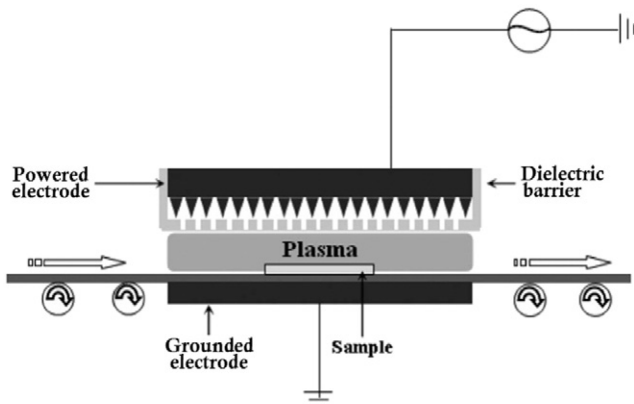

Fig. 29. Schematic diagram of a multi-pin DBD atmospheric plasma in-line system [74].

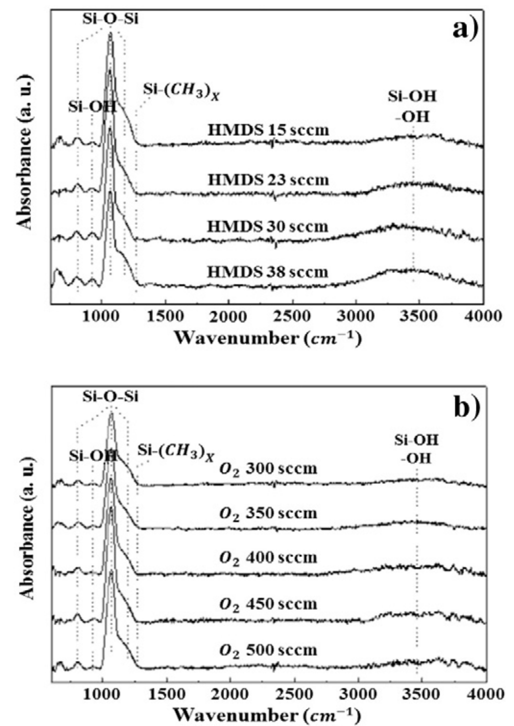

Fig. 30. FTIR spectra of SiO_x films deposited by atmospheric pressure PECVD with varying flow rates of (a) HDMS and (b) O_2. [74] The HDMS flow rates were varied from 15 to 38 sccm at constant O_2 flow rate of 300 sccm and O_2 flow rates were varied from 300 to 500 sccm at constant HDMS flow rate of 15 sccm. 2 slm of Ar flow rate was used to activate atmospheric-pressure plasma. Six hundred nm was deposited to measure the FTIR spectra.

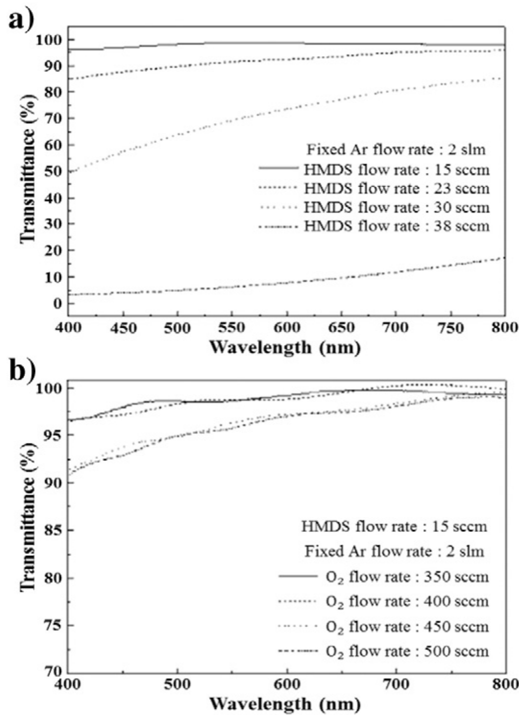

Fig. 31. Optical transmittance spectra of SiO_x films deposited by atmospheric-pressure PECVD with varying flow rates of (a) HDMS and (b) O_2 gas [74]. The deposition conditions are the same as0 those in Fig. 30.

grid structures for organic light emitting diodes (OLEDs), and organic photovoltaics (OPV) integrated into roll-to-roll production.

3.4. Deposition on plastic substrates

Inorganic thin films such as SiO_2 find applications in the field of flexible electronics as a diffusion barrier material in organic electronics including OLEDs, organic thin-film transistors (OTFTs), flexible displays, etc., all of which are vulnerable to environmental degradation. SiO_2 thin films have been also deposited on polydimethylsiloxane (PDMS) to modify the surface from being inherently hydrophobic to becoming a stable hydrophilic surface used in various lab-on-a-chip devices. In general, the thin film barrier layers are deposited by low-pressure plasma enhanced CVD (LP-PECVD) to lower the deposition temperature. However, atmospheric-pressure plasma-enhanced CVD (AP-PECVD) deposition of inorganic thin film has advantages over LP-PECVD including the fact that a loadlock system is not required and there is no limit on the size of the processing chamber and conformal coatings can be obtained on very large area substrates.

For high rate deposition of inorganic thin film using AP-PECVD, a modified atmospheric DBD system, illustrated in Figs. 29 and in 1(d), has been used to deposit SiO_x film on plastic substrates at low temperature <50 °C in Ar/HMDS/O_2 gas mixtures. [74] HMDS was used as the silicon precursor, oxygen as the oxidizing agent, and Ar as the ignition and carrier gas. The characteristics of as-deposited SiO_x thin films have been investigated as functions of HDMS and O_2 flow rates, and the results

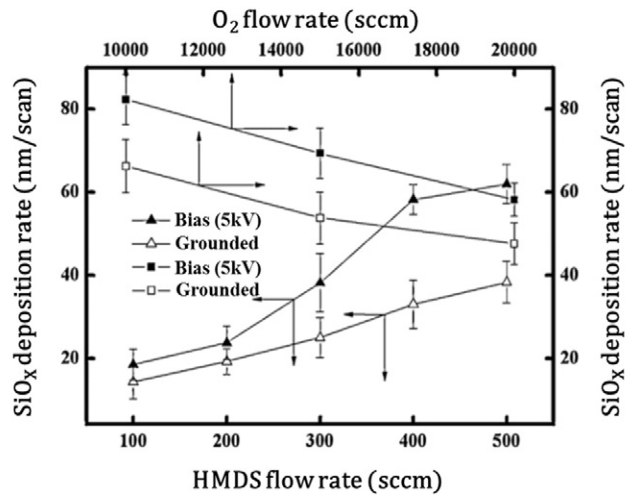

Fig. 33. Deposition rates of SiO_x thin films as a function of HMDS and O_2 flow rates in a gas mixture of HMDS (varied)/O_2 (varied)/He (5 slm)/Ar (3 slm) at an applied voltage to the remote DBD of 7 kV (30 kHz). The substrate was grounded or AC biased at 5 kV (20 kHz) (to form a direct DBD in addition to the remote DBD, that is, for the double-discharge DBD). Silicon wafers or PCs were used as the substrates [13].

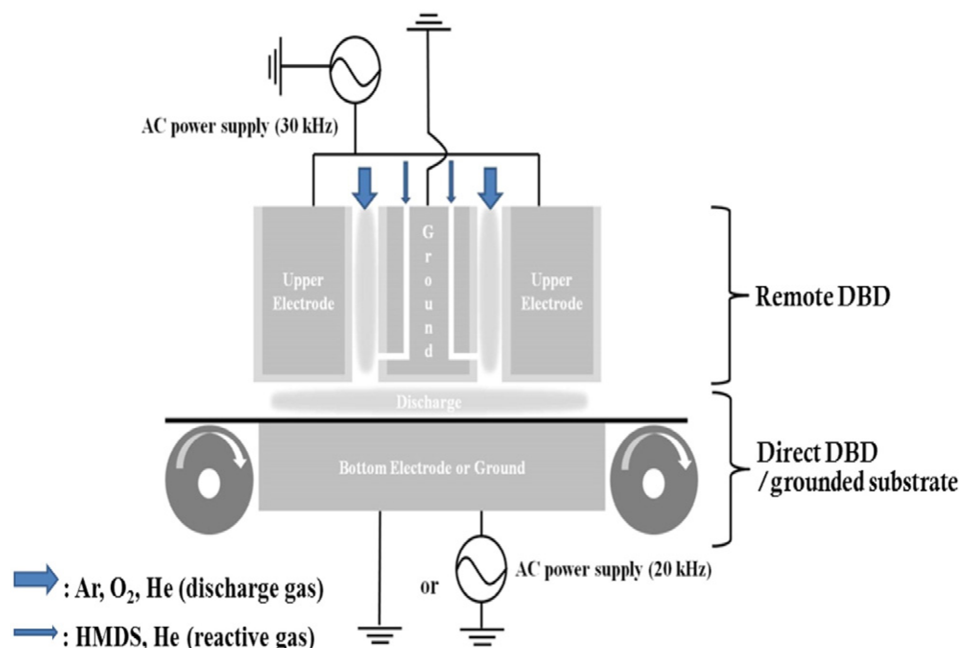

Fig. 32. A double discharge system composed of a remote DBD on the top and a direct DBD at the bottom (by applying AC pulse power to the substrate) [13].

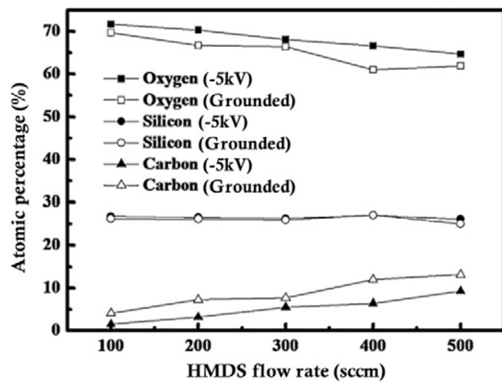

Fig. 34. SiO_x atomic percentage determined by XPS in thin films deposited by combined remote/direct DBD (see Fig. 32) as a function of the HMDS flow rate for the conditions listed in Fig. 33. The substrate was grounded for a remote DBD configuration or AC biased at 5 kV (20 kHz) for the double-discharge configuration [13].

based upon Fourier transform infrared spectroscopy (FTIR) and optical transmittance are shown in Figs. 30 and 31, respectively. A decrease in Si–O–Si bonding with corresponding increase Si–OH bonding was observed with increasing HDMS flow rate while keeping the gas flow rates of Ar (2 slm) and O_2 (300 sccm) as shown in Fig. 30(a). The observed increase in Si–OH bonding was speculated to be the result of incomplete dissociation/oxidation of HMDS due to the high HMDS flow rates. When the oxygen flow rate was increased at a fixed HMDS flow rate of 15 sccm, as shown in Fig. 30(b), an increase in Si–O–Si bonding could was observed up to 450 sccm, likely due to further dissociation and oxidation of HMDS in the gas mixture. However, a further increase in the oxygen flow rate to 500 sccm showed no further increases in Si–O–Si bonding peak, indicating complete HMDS dissociation and oxidation. The optical transmittance of the deposited SiO_x thin film also varied with HMDS and O_2 flow rates. As can be seen from Fig. 31(a), the highest optical transmittance (>95%) was obtained at the lowest HMDS flow rate (15 sccm). The optical transmittance decreased with increasing HMDS flow rate, due to scattering by white bubble-like particles caused by the incomplete dissociation/oxidation of HMDS. The optical transmittance increases with increasing O_2 flow rate and reaches a maximum at 400 sccm as shown in Fig. 31(b) due to the increased dissociation and oxidation of HMDS. In addition, film compositions, as determined by X-ray photoelectron spectroscopy (XPS), were close to stoichiometric SiO_2 for the films grown at low HDMS and high O_2 flow rates. Therefore, by using an optimum gas mixture of Ar/HMDS/O_2, a smooth and optically transparent thin film similar to SiO_2 deposited by low-pressure PECVD can be obtained by AP-PECVD using the modified DBD source.

A common problem in AP-DBD systems is substrate damage due to the formation of filamentary discharges, especially at high powers used for high deposition rates or with high oxygen flow rates used to deposit stoichiometric SiO_2. Substrate damage can be avoided by using remote AP-DBD systems as shown in Fig. 1(c). However, remote AP-DBD systems typically provide low deposition rates even when modified for higher plasma densities as in Fig. 1(e). Therefore, a double-discharge DBD system has been proposed [13]; it is composed of a combined remote DBD and direct DBD source (grounded for a remote DBD configuration or pulse/AC voltage applied to the substrate in addition to the remote DBD for the double-discharge configuration) as illustrated in Figs. 32(a) and 1(f). Using a double-discharge DBD source, nearly stoichiometric SiO_2-like thin films have been deposited at high rates in gas mixtures composed of HMDS/O_2/He/Ar. The remote-DBD was operated at 7 kV AC voltage (30 kHz) and the direct DBD at 5 kV AC voltage (20 kHz). The plastic or glass substrate translation

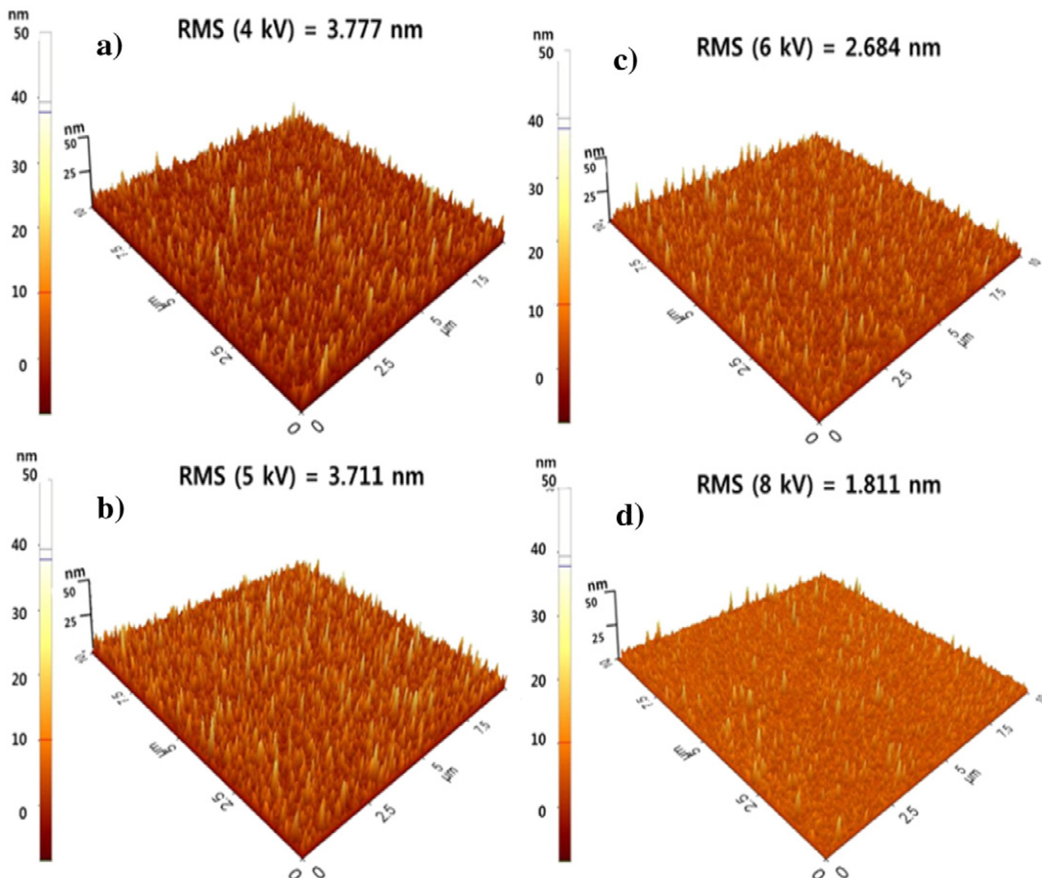

Fig. 35. AFM surface roughness of SiO_x thin films deposited as a function of AC voltage to the silicon substrate. A gas mixture of HMDS (400 sccm)/O_2 (20 slm)/He (5 slm)/Ar (3 slm) was used to deposit SiO_x. A 7 kV of AC voltage at 30 kHz was applied to the remote DBD while the substrate electrode was AC biased from 4 to 8 kV at 20 kHz [14].

velocity was 0.3 m/min. As can be seen in Fig. 33, the deposition rate on grounded polymer or glass substrates increased with HMDS flow rate due to an increases in the gas mixture Si source and decreased with O_2 flow rate due to the decrease of HMDS percentage in the gas mixture (that is, even though the HMDS flow rate is the same, due to the increase of total flow rate, the HMDS percentage in the gas mixture is decreased) and a decrease in the plasma density (oxygen decreases the plasma electron concentrations by forming negative ions) similar to the other DBD sources. However, instead of grounding the substrate holder, when the substrate holder was AC biased at 5 kV and 20 kHz for the direct DBD, due to the formation of the additional plasma above the substrate, the deposition rate was significantly increased by the additional dissociation of molecules near the substrate without forming filamentary discharges.

Fig. 34 shows the atomic percentages of SiO_x thin films, determined by XPS, deposited by the double-discharge DBD system with the substrates either grounded (for a remote DBD configuration) or AC biased at 5 kV 20 kHz (for the double-discharge DBD by forming additional direct DBD above the substrate). Increasing HMDS flow rate with grounded substrate decreased oxygen and increased carbon concentrations due to incomplete oxidation and dissociation, while not significantly changing the silicon percentage. However, applying 5 kV 20 kHz AC voltage to the substrate (that is, by forming the double-discharge DBD) increased the oxygen and decreased the carbon concentrations while having no effect on silicon concentration. Therefore, the use of the double-discharge DBD resulted not only in increased deposition rates, without filamentary discharge damage, but the films had concentrations closer to stoichiometric SiO_2.

In the double-discharge DBD system, Gil et al. [14] demonstrated that the direct DBD formed on the substrate has a significant influence on the smoothness and hardness of SiO_x thin films deposited on silicon wafers as shown in Figs. 35 and 36(a), respectively. The hardness of the SiO_x thin film was measured using a commercially available nanoindentation instrument (MTS, Nano-indenter II) with a normal load of 30 mN. As shown in Fig. 35, the increase of the direct DBD voltage applied to the substrate decreased the RMS surface roughness of SiO_x deposited on the silicon wafers. In addition, as shown in Fig. 36(a), the increase of the bias voltage to the substrate increased the hardness of the SiO_x deposited on the silicon substrate. Therefore, by forming direct DBD by applying AC voltage directly to the substrate in addition to the remote DBD, that is by forming the double-discharge DBD, there is not only an improvement in the RMS surface roughness, but also increased hardness of the deposited SiO_x is observed. These improvements were also related to increased HMDS dissociation and oxidation due to the increased plasma density near the substrate by forming the additional plasma near the substrate. FTIR measurements (not shown) reveal a decrease in carbon incorporation with increasing AC bias voltage more likely due to the increased CO_x formation and desorption. However, the results Fig. 32(b) indicate that the application and increase of AC bias voltage to the substrate also increases the ion bombardment to the substrate and promotes surface reaction rates by adding extra energy on the surface.

At the atmospheric pressure, even though the mean free path of the ions is only several tens of nanometers, the application of AC bias voltage can increase surface reaction rates by adding extra energy on the surface through the ion bombardment during the negative AC voltage cycle applied to the substrate. The effect of ion bombardment by the application of AC voltage directly to the substrate during the double-discharge DBD was investigated. As shown in the inset of Fig. 36(b), the silicon substrate was located about 200 μm above the AC biased electrode (floating substrate) and SiO_x was deposited with the same process conditions as shown in Fig. 36(a). For the substrate directly in contact with the AC voltage in Fig. 36(a), the substrate is bombarded by the ion energy due to the high negative voltage during the negative AC cycle. However, for the substrate located above the AC electrode in Fig. 36(b), the substrate is not bombarded with ion energy due to no AC voltage in contact with the substrate. However, in both cases, the additional direct DBD was formed above the substrate; therefore, increased plasma density is obtained which increases the HMDS dissociation and oxidation except for ion bombardment effect. As shown in Fig. 36(b), even though the AC voltage to the substrate electrode is increased, no significant change in the hardness of the deposited SiO_x thin film different from those in Fig. 36(a) was observed indicating no change of ion bombardment energy with increasing AC voltage. Therefore, when the double-discharge DBD with the configuration shown in Fig. 32 is used, the improvement in surface roughness and hardness of SiO_x shown in Figs. 35 and 36(a) during the double-discharge DBD is at least partially related to ion bombardment during SiO_2 deposition.

As mentioned above, SiO_x thin films have also been deposited on PDMS to form stable hydrophilic surfaces. PDMS is widely used for the microfabrication of variety of lab-on-a-chip devices due to properties such optical transparency, high elasticity, etc. Recently, it has been demonstrated that patterned PDMS can act as a pressure-sensitive capacitor array integrated in indium tin oxide (ITO)/PET gate dielectrics on organic FET arrays [75]. However, PDMS is inherently hydrophobic and it is not favorable in some applications such as binding of biomolecules by physical adsorption, electro-osmotic flow applications for lab-on-a-chip, etc. Therefore, for these applications, it is necessary to modify the surface properties of PDMS to be hydrophilic. Using APPs, several attempts have been made to render the PDMS surface hydrophilic [76–78]. Oxygen-based plasma treatment is a simple and commonly used means of making the PDMS surface hydrophilic, but the hydrophilicity is soon lost because PDMS oligomers migrating from the bulk to the air–surface interface cause hydrophobic recovery within a few hours following the plasma treatment. D. Lee et al. [78] used AP-PECVD to deposit a bilayer consisting of a hydrocarbon (C:H) using CH_4 as a precursor gas and SiO_x using TEOS/O_2 in a AP-PECVD system based upon an

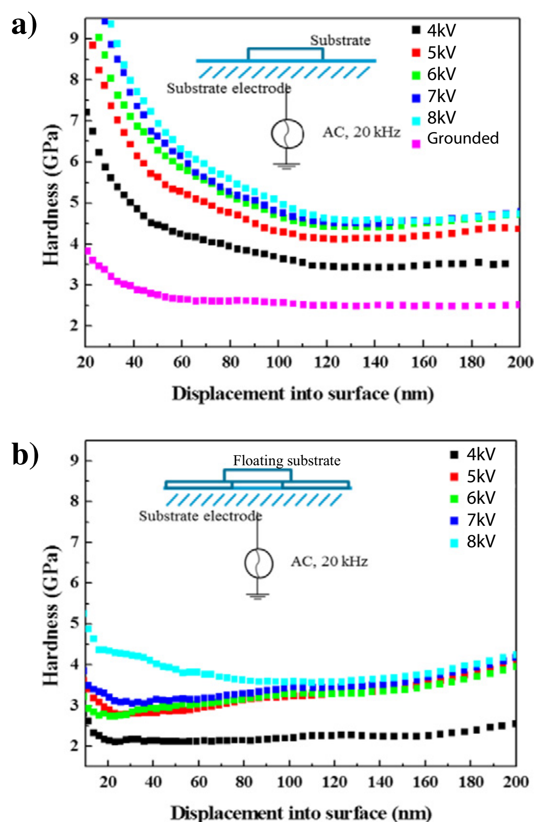

Fig. 36. Hardness of deposited SiO_x as a function of AC bias voltage to the substrate. The thickness of SiO_x was kept constant at 300 nm. SiO_x thin films were deposited (a) on the silicon substrate attached to the AC biased electrode and (b) on the silicon substrate floated about 200 μm above AC biased electrode with a polymer spacer. The deposition conditions are the same as those in Fig. 35 [14].

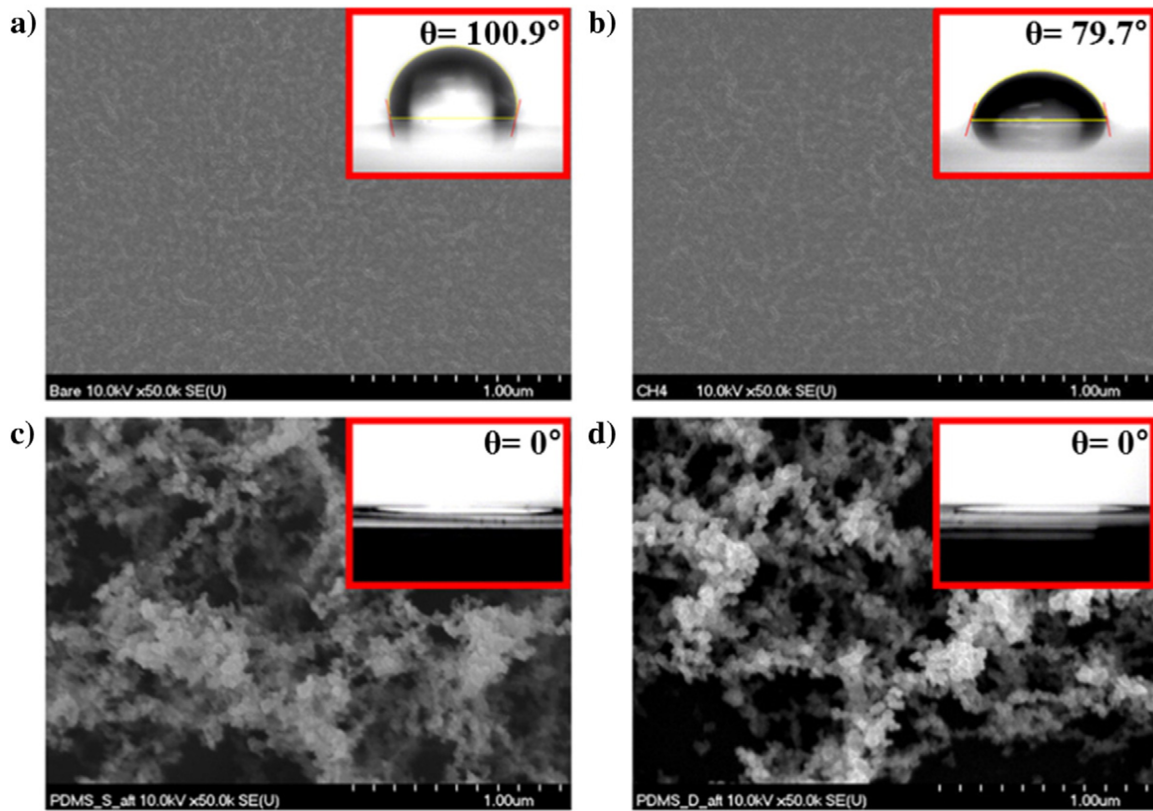

Fig. 37. SEM images at 50,000× magnification and static contact angle θ for (a) unmodified PDMS (b) CH_4/PDMS (c) TEOS-O_2/PDMS and (d) TEOS-O_2/CH_4/PDMS. [78] The experiments have been carried out in an atmospheric pressure PECVD system operated at 13.56 MHz and a power of 200 W. CH_4 (5%) was mixed with argon for the hydrocarbon layer deposition, while a mixture of TEOS (vaporized by 1 slm of argon) and O_2 was used for depositing the hydrophilic SiO_x layer. Helium was used as the carrier gas (15 slm for AP-PECVD with CH_4; 5–15 slm for AP-PECVD with TEOS-O_2).

APPJ device as illustrated in Fig. 2, operated with a 13.56 MHz RF power. 5% of CH_4 mixed with argon was used as the reactant for the C:H layer deposition, while a mixture of TEOS (vaporized by 1 slm of argon) and O_2 was used for depositing the hydrophilic SiO_x layer on the C:H layer. Helium was used as the carrier gas (15 slm for AP-PECVD with CH_4; 5–15 slm for AP-PECVD with TEOS-O_2). An rf power of 200 W was employed for plasma deposition. The distance between the nozzle head of the APPJ and the sample was adjusted to 1.5 mm for the C:H layer deposition and 2 mm for the hydrophilic SiO_x layer deposition. The samples were mounted on a moving stage positioned below the APPJ; the stage moved at a speed of about 20 mm/s in the orthogonal direction with respect to the plasma source head. The substrate was repeatedly passed back and forth across the plasma head region.

The highly cross-linked C:H interlayer (about 100 nm thick) acted as a physical barrier layer which suppresses the hydrophobic recovery of the modified PDMS surface between the bare PDMS surface and the hydrophilic SiO_x overlayer. SEM images of the PDMS surfaces are shown in Fig. 37 with the static contact angle images measured on the day of surface modification. As shown in the SEM images of Fig. 37, the unmodified PDMS and the C:H layer on PDMS (CH_4/PDMS) showed smooth surfaces while the SiO_x layer on PDMS (TEOS-O_2/PDMS) and the SiO_x layer/C:H layer on PDMS(TEOS-O_2/CH_4/PDMS) samples showed rough surfaces. The rough surface roughness after the deposition of SiO_x by TEOS-O_2 for the TEOS-O_2/PDMS and TEOS-O_2/CH_4/PDMS samples in Fig. 37(c) and (d) is related to the TEOS-O_2 coating layer composed of hydrophilic SiO_x particles on the surface during the plasma jetting. As shown in the contact angle measurement, after the contact angle was high for the TEOS-O_2/PDMS and TEOS-O_2/CH_4/PDMS samples but, after the SiO_x deposition, the contact angle was decreased to near 0°. The change of contact angle with time was investigated to determine long term stability of the hydrophilic surfaces and the results are presented in Fig. 38 for the samples shown in Fig. 37. The SiO_2 deposited directly on PDMS (TEOS-O_2/PMDS) showed the recovery to hydrophobicity due to the diffusion of PDMS oligomers to the surface. By depositing a C:H layer using CH_4 between SiO_2 and PDMS, the hydrophilicity degradation could be prevented over a period of 28 days after AP-PECVD by blocking the diffusion of PDMS oligomers to the surface.

4. Conclusion

The primary types of atmospheric pressure plasma (APP) sources, together with possible applications, have been described. APPs offer various advantages over other type of plasma sources for surface

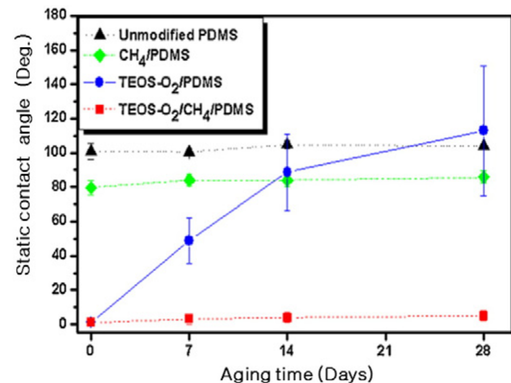

Fig. 38. Plots of static contact angle measured 0, 7, 14, and 28 days after surface modification: comparison of unmodified PDMS, CH_4/PDMS, TEOS-O_2/PDMS, and TEOS-O_2/CH_4/PDMS [78].

processing of flexible materials due to the absence of vacuum equipment, which results in several benefits such as the reduction of process and reactor costs, less complex deposition systems, and easier process integration into continuous (e.g., roll-to-roll) production lines. Among the various types of APPs, direct barrier discharge (DBD) APPs are widely used and investigated for surface modification, surface texturing, and sintering processes of the materials deposited on flexible substrates. APPs have also been applied to low temperature deposition of thin SiO_x films on flexible polymer substrates for use as diffusion barrier and stable hydrophilic surfaces. Due to the advantages listed above, it is believed that more applications, including wearable electronics and organic electronics on flexible polymer substrates, will emerge in the near future.

Acknowledgments

This work was supported by the Industrial Strategic Technology Development program (10041926, Development of high-density plasma technologies for thin-film deposition of nanoscale semiconductors and flexible display processing) funded by the Ministry of Knowledge Economy (MKE, Korea) and was also supported by the MOTIE (Ministry of Trade, Industry & Energy (10049065) and KSRC (Korea Semiconductor Research Consortium) support program for development of future semiconductor devices.

References

[1] R.F. Service, Science 278 (1997) 383.
[2] K. Kim, J. Bang, Y. Choa, S. Jung, Microelectron. Eng. 107 (2013) 121.
[3] L. Bárdos, H. Baránková, Thin Solid Films 518 (2010) 6705.
[4] D. Merche, N. Vandencasteele, F. Reniers, Thin Solid Films 520 (2012) 4219.
[5] F. Fanelli, Surf. Coat. Technol. 205 (2010) 1536.
[6] J.B. Park, S.J. Kyung, G.Y. Yeom, Plasma Proc. Nanomater. 165 (2011).
[7] U. Kogelschatz, Plasma Chem. Plasma Process. 23 (2003) 1.
[8] J.R. Roth, J. Rahel, X. Dai, D.M. Sherman, J. Phys. D 38 (2005) 555.
[9] O. Sakai, Y. Kishimoto, K. Tachibana, J. Phys. D 38 (2005) 431.
[10] J. Park, J. Oh, E. Gil, S. Kyoung, J. Lim, G. Yeom, J. Electrochem. Soc. 157 (2010) D614.
[11] J.B. Park, J.Y. Choi, S.H. Lee, Y.S. Song, G.Y. Yeom, Soft Matter 8 (2012) 5020.
[12] J.B. Park, J.S. Oh, E. Gil, S. Kyoung, J. Kim, G.Y. Yeom, J. Phys. D 42 (2009) 215201.
[13] J. Park, J. Oh, E. Gil, G.Y. Yeom, Mater. Res. Bull. 47 (2012) 3011.
[14] E. Gil, J.B. Park, J.S. Oh, M.S. Jhon, G.Y. Yeom, J. Electrochem. Soc. 158 (3) (2011) G58.
[15] A. Fridman, A. Chirokov, A. Gutsol, J. Phys. D 38 (2005) R1.
[16] A. Fridman, Plasma Chemistry, Cambridge University Press, 2008.
[17] J.L. Walsh, F. Iza, N.B. Janson, V. Law, M.G. Kong, J. Phys. D 43 (2010) 075201.
[18] J. Jeong, S. Babayan, V. Tu, J. Park, I. Henins, R. Hicks, G. Selwyn, Plasma Sources Sci. Technol. 7 (1998) 282.
[19] G. Kim, G. Kim, S. Park, S. Jeon, H. Seo, F. Iza, J. Lee, J. Phys. D: Appl. Phys 42 (2009) 1.
[20] D. Dobrynin, G. Fridman, G. Friedman, A. Fridman, New J. Phys. 11 (2009) 115020.
[21] G. Kim, W. Kim, K. Kim, J. Lee, Appl. Phys. Lett. 96 (2010) 021502.
[22] J.Y. Kim, S. Kim, Y. Wei, J. Li, Appl. Phys. Lett. 96 (2010) 203701.
[23] S.J. Kim, T. Chung, S. Bae, S. Leem, Appl. Phys. Lett. 97 (2010) 023702.
[24] C. Tendero, C. Tixier, P. Tristant, J. Desmaison, P. Leprince, Spectrochim. Acta Part B At. Spectrosc. 61 (2006) 2.
[25] H. Koinuma, H. Ohkubo, T. Hashimoto, K. Inomata, T. Shiraishi, A. Miyanaga, S. Hayashi, Appl. Phys. Lett. 60 (1992) 816.
[26] K. Inomata, H. Koinuma, Y. Oikawa, T. Shiraishi, Appl. Phys. Lett. 66 (1995) 2188.
[27] K. Inomata, H. Ha, K.A. Chaudhary, H. Koinuma, Appl. Phys. Lett. 64 (1994) 46.
[28] H. Ha, K. Inomata, H. Koinuma, J. Electrochem. Soc. 142 (1995) 2726.
[29] H. Ha, M. Yoshimoto, H. Koinuma, B. Moon, H. Ishiwara, Appl. Phys. Lett. 68 (1996) 2965.
[30] H. Ha, B. Moon, T. Horiuchi, T. Inushima, H. Ishiwara, H. Koinuma, Mater. Sci. Eng. B 41 (1996) 143.
[31] A. Schutze, J.Y. Jeong, S.E. Babayan, J. Park, G.S. Selwyn, R.F. Hicks, IEEE Trans. Plasma Sci. 26 (1998) 1685.
[32] M. Goldman, R. Sigmond, IEEE Trans. Dielectr. Electr. Insul. 36 (1982) 90.
[33] Y.P. Raizer, V.I. Kisin, J.E. Allen, Gas Discharge Physics, Springer-Verlag, Berlin, 1991.
[34] J.M. Meek, J.D. Craggs, 1978.
[35] M. Laroussi, IEEE Trans. Plasma Sci. 30 (2002) 1409.
[36] U. Kogelschatz, B. Eliasson, Handbook of Electrostatic Processes5811995.
[37] K. Gerstenberg, Mater. Sci. Eng. A 139 (1991) 110.
[38] O. Greenwood, R. Boyd, J. Hopkins, J. Badyal, J. Adhes. Sci. Technol. 9 (1995) 311.
[39] Y. Park, K. Choi, H. Kim, Electrochem. Solid-State Lett. 12 (2009) H426.
[40] Y. Zeng, Z. Ye, W. Xu, B. Liu, Y. Che, L. Zhu, B. Zhao, Mater. Lett. 61 (2007) 41.
[41] F. Zhuge, L. Zhu, Z. Ye, J. Lu, H. He, B. Zhao, Chem. Phys. Lett. 437 (2007) 203.
[42] S.H. Cha, M.S. Oh, K.H. Lee, S. Im, B.H. Lee, M.M. Sung, Appl. Phys. Lett. 92 (2008) 023506.
[43] D. Kang, H. Lim, C. Kim, I. Song, J. Park, Y. Park, J. Chung, Appl. Phys. Lett. 90 (2007) 192101.
[44] J.W. Jung, Y.W. Song, H.G. Nam, N.I. Cho, J. Korean Phys. Soc. 56 (2010) 388.
[45] T. Homola, J. Matoušek, B. Hergelová, M. Kormunda, L.Y. Wu, M. Černák, Polym. Degrad. Stab. 97 (2012) 2249.
[46] M.S. Fleischman, B.S. Lee, V. Rodriguez-Santiago, V. Chhasatia, Y. Sun, D.D. Pappas, Surf. Coat. Technol. 206 (2012) 3923.
[47] E. Gonzalez II, M.D. Barankin, P.C. Guschl, R.F. Hicks, Plasma Process. Polym. 7 (2010) 482.
[48] E. Gonzalez, R.F. Hicks, Langmuir 26 (2009) 3710.
[49] A. Oravcova, I. Hudec, Acta Chim. Slov. 3 (2010) 57.
[50] K. Kostov, T. Nishime, L. Hein, A. Toth, Surf. Coat. Technol. 234 (2013) 60.
[51] Z. Gao, J. Sun, S. Peng, L. Yao, Y. Qiu, Appl. Surf. Sci. 256 (2009) 1496.
[52] B. Kafle, D. Torgus, B. Dresler, D. Kohler, G. Mader, L. Clochard, E. Duffy, M. Hofmann, J. Rentsch, Anonymous Industrial Screen Printed Solar Cells with Novel Atmospheric Pressure Dry Texturing Process, paris, 2013.
[53] J. Hodgkinson, M. Thomson, I. Cook, D. Sheel, J. Nanosci. Nanotechnol. 11 (2011) 8403.
[54] S. Wünscher, S. Stumpf, J. Perelaer, U.S. Schubert, J. Mater. Chem. C 2 (2) (2014) 1642.
[55] T.H. Van Osch, J. Perelaer, A.W. de Laat, U.S. Schubert, Adv. Mater. 20 (2008) 343.
[56] D. Soltman, V. Subramanian, Langmuir 24 (2008) 2224.
[57] S. Wünscher, S. Stumpf, A. Teichler, O. Pabst, J. Perelaer, E. Beckert, U.S. Schubert, J. Mater. Chem. 22 (2012) 24569.
[58] A. Kamyshny, J. Steinke, S. Magdassi, TOAPJ 4 (2011) 19.
[59] S. Magdassi, A. Bassa, Y. Vinetsky, A. Kamyshny, Chem. Mater. 15 (2003) 2208.
[60] J. Perelaer, A.W. de Laat, C.E. Hendriks, U.S. Schubert, J. Mater. Chem. 18 (2008) 3209.
[61] I. Reinhold, C.E. Hendriks, R. Eckardt, J.M. Kranenburg, J. Perelaer, R.R. Baumann, U.S. Schubert, J. Mater. Chem. 19 (2009) 3384.
[62] J. Park, S. Baek, Scr. Mater. 55 (2006) 1139.
[63] K. Chou, K. Huang, H. Lee, Nanotechnology 16 (2005) 779.
[64] G.G. Rozenberg, E. Bresler, S.P. Speakman, C. Jeynes, J.H. Steinke, Appl. Phys. Lett. 81 (2002) 5249.
[65] S.H. Ko, H. Pan, C.P. Grigoropoulos, C.K. Luscombe, J.M. Fréchet, D. Poulikakos, Appl. Phys. Lett. 90 (2007) 141103.
[66] R. Roy, D. Agrawal, J. Cheng, S. Gedebanishvili, Nature 399 (1999) 668.
[67] J. Perelaer, B. de Gans, U.S. Schubert, Adv. Mater. 18 (2006) 2101.
[68] J.R. Groza, S.H. Risbud, K. Yamazaki, J. Mater. Res. 7 (1992) 2643.
[69] J.M. Lourenço, A.M. Maliska, A.N. Klein, J.L.R. Muzart, Mater. Res. 7 (2004) 269.
[70] A. Maliska, H. Pavanati, A. Klein, J. Muzart, Mater. Sci. Eng. A 352 (2003) 273.
[71] J. Perelaer, C.E. Hendriks, A.W. de Laat, U.S. Schubert, Nanotechnology 20 (2009) 165303.
[72] M.L. Allen, M. Aronniemi, T. Mattila, A. Alastalo, K. Ojanperä, M. Suhonen, H. Seppä, Nanotechnology 19 (2008) 175201.
[73] S. Jang, Y. Seo, J. Choi, T. Kim, J. Cho, S. Kim, D. Kim, Scr. Mater. 62 (2010) 258.
[74] J. Lee, T.T. Pham, Y. Kim, J. Lim, S. Kyung, G. Yeom, J. Electrochem. Soc. 155 (2008) D163.
[75] J.J. Boland, Nat. Mater. 9 (2010) 790.
[76] N. Kim, S. Hong, S. Park, Y. Hong, Anonymous Journal of Physics: Conference Series, 34, IOP Publishing 2006, p. 650.
[77] H.T. Kim, O.C. Jeong, Microelectron. Eng. 88 (2011) 2281.
[78] D. Lee, S. Yang, Sensors Actuators B Chem. 162 (2012) 425.